UNIVERSITY OF CALIFORNIA SAN DIEGO

Study of Insulator Related Effects on Pinch Dynamics and Structure in a 10 kJ Dense Plasma Focus

A thesis submitted in partial satisfaction of the requirements for the degree Master of Science

in

Engineering Sciences (Engineering Physics)

by

David Benjamin Housley

Committee in charge:

Professor Farhat N Beg, Chair
Professor Alexey Arefiev
Professor Veronica Eliasson

2020

The thesis of David Benjamin Housley is approved, and it is acceptable in quality and form for publication on microfilm and electronically:

Chair

University of California San Diego

2020

Table of Contents

List of Abbreviations

Al	Aluminum
ASD	Atomic Spectral Database
Cu	Copper
DPF	Dense Plasma Focus
EM	Electromagnetic
FWHM	Full-Width, Half Maximum
LTE	Local Thermodynamic Equilibrium
Nd:YAG	Neodymium-doped Yttrium Aluminum Garnet
Ne	Neon
NIST	National Institute of Standards and Technology
PIN	P-type, Intrinsic, N-type
PTFE	Polytetrafluoroethylene
Si	Silicon
UCSD	University of California, San Diego
XUV	Extreme ultraviolet radiation

List of Symbols

Symbol	Definition	Units
A	atomic number	unit less
a	anode radius	cm
b	cathode radius	cm
C	capacitance	F
I	current	kA
L	inductance	H
n_e	electron density	cm^{-3}
P_0	fill gas pressure	torr
R	resistance	Ω
t	time	s
T_e	electron temperature	eV
V_0	charging voltage	kV
z	anode length	cm
λ	wavelength	nm

List of Figures

List of Tables

Acknowledgements

I thank Dr. Farhat Beg for his support and encouragement in my research and writing. I would also like to thank the HEDP research group at CER for their insights into the field, their patience with my unending questions, and the strength I gain from their examples and camaraderie.

I thank my wife and mother-in-law for their unfailing interest and support of my efforts, and my daughters for their enthusiasm. Most of all I would like to thank my Father in Heaven for His support and encouragement.

This project has been generously supported by the Air Force Office of Scientific Research announcement FA9550-18-S-0003.

Fruitful discussions with Mahadevan Krishnan and assistance with DPF operation from Swarvanu Gosh are greatly appreciated.

This thesis, in part is currently being prepared for submission for publication of the material. Housley, David; Hahn, Eric N.; Conti, Fabio; Narkis, Jeff; Beg, Farhat, N. The thesis author was the primary investigator and author of this material.

ABSTRACT OF THE THESIS

Study of Insulator Related Effects on Pinch Dynamics and Structure in a 10 kJ Dense Plasma Focus*

by

David Benjamin Housley

Master of Science in Engineering Sciences (Engineering Physics)

University of California San Diego, 2020

Professor Farhat Beg, Chair

The Dense Plasma Focus (DPF) is a Z-pinch configuration that can produce intense bursts of energetic particles (electrons, ions and neutrons) and X-rays. This makes DPF attractive for applications where intense X-rays and energetic particles are needed. However, significant variation between shots is a challenge. Here we detail experiments on a 4.4 kJ DPF (250 kA current, 2.5 μs rise time) using neon fill gas that demonstrate the critical role of insulator surface conditioning on pinch structure, dynamics, and X-ray yield. This is accomplished through same-shot imaging of the evolving plasma sheath during breakdown, rundown, and at the pinch with X-ray sensitive photodiodes. Smooth surfaces on the borosilicate glass insulators demonstrate the highest X-ray production whereas conditioning

the insulator surface with micro-scratches or machined grooves reduces X-ray signals by a factor of 4 on average. Specifically, horizontal exterior surface structures were shown to decrease the yield by a factor of six, whereas vertical structures on the exterior surface and interior horizontal structures both decreased the X-ray yield two fold. Small differences in sheath liftoff timing are measured on the order of ~100 ns. Sheath asymmetry and inhomogeneity at liftoff are observed, suggesting that local variations in surface structuring decrease the uniformity of the sheath, ultimately leading to reduced performance. This is likely due to the disruption of electron flow over the modified surface as the insulator flashes over and the inherently higher azimuthal variability in the local structure of modified surfaces.

*Research supported by Air Force Office of Scientific Research grant FA9550-18-S0003.

Chapter 1 Introduction and Theory

Dense Plasma Focus (DPF), a Compact Neutron/X-ray/Ion Source

The DPF is a compact, intense source of x-rays, neutrons, and energetic charged

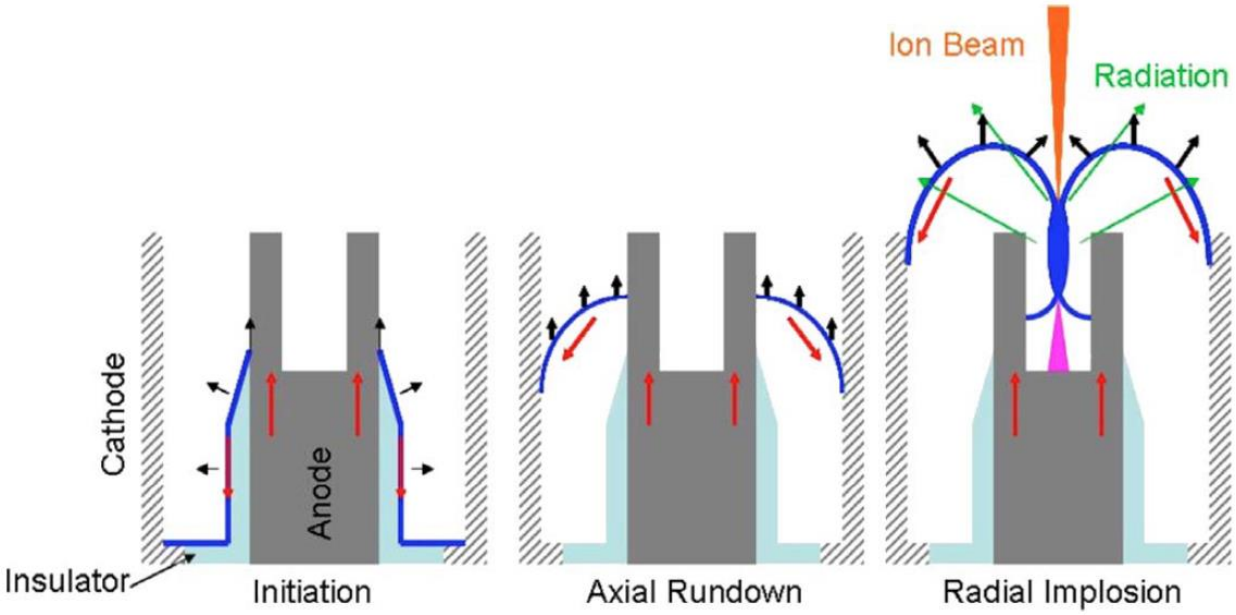

Figure 1. Sheath progression in the operation of DPF showing initiation or breakdown (left), rundown (center) and radial or implosion (right) phases. The insulator is represented in light blue separating the anode (grey) and cathode (diagonally striped gray). The current direction shown with red arrows, JxB force of the sheath noted by black arrows, ion and electron beams drawn in orange and pink and photon radiation noted in green[2].

particles. The high conversion efficiency of the stored electrical energy makes the DPF an attractive source choice. The DPF is comprised of a set of coaxial electrodes separated by an insulator in a background gas (see Figure 1). Flashover of the insulator separating the electrodes initiates the formation of a plasma sheath that conveys current between the two electrodes during operation. The development of the current gives rise to a magnetic field which in turn results in a force on the mobile charges. Subsequently the plasma sheath drifts toward the open end of the electrodes, turns inward, and pinches on axis. As the sheath drifts through the fill gas it accumulates mass (increasing its density)[1].

Typical sheath drift speeds observed in the run-down phase are approximately 100 km/s and in the radial phase often reach as high as 250 km/s[2]. The sheath forms a pinch on axis resulting in a hot (~1eV), dense (~10^{19} cm^{-3}) plasma and can result in the emission of X-rays, energetic ions, electrons, and dependent on the fill gas employed, neutrons[2,3,4,5].

The effect of insulator material

Optimization efforts frequently focus on the electrode geometry and power flow of the system[6,7,8]. Additionally, many studies have been dedicated to evaluating the influence of insulator sleeve material, and thus its electrical/mechanical properties, on the yield of DPF devices[9,10,11]. These studies have investigated the effect of different insulator sleeve materials on neutron yield[10] and X-ray yield[12] suggesting that yield is correlated with the intrinsic properties of the insulator—the dielectric strength for neutrons or the surface resistivity for X-rays respectively. The latter study speculates that the higher resistivity of the insulator reduces leakage current between the electrodes at the time of the pinch, coupling more of the energy to the pinch resulting in higher plasma temperatures, 3.6 keV vs. 3 keV for the 10^{16} Ω fused silica and 10^{15} Ω Pyrex respectively. An intriguing insight into the operation of DPFs with different insulator and electrode combinations is detailed by Shyam and Rout[9], where they were able to measure localized current via Rogowski coils and infer the speed and uniformity of the sheath and subsequently an effective impurity level of the plasma sheath. They demonstrated that plastic-based insulator sleeves produce non-uniform sheaths that move much slower due to a high level of contaminants in the sheath, attributing lack of neutron yield to both the non-uniformity and radiative effects of the contaminant ions. It was demonstrated that ceramic insulator sheaths result in significantly less atomic contamination levels (resulting from the emission of metal vapor from the anode) on the order of 1% for a copper anode and a glass

insulator. The authors conjectured that differences in insulator material surface properties result in different amounts of metallic surface deposition, leading to greater leakage current for Alumina compared to either quartz or glass.[9]

Insulator surface effects

There has been little study of the surface finish of insulator materials as it pertains to reproducibility and optimization of yield. An early work by Feugeas[13] showed that metal vapor deposits (1 μm in size) correlated to an increase in current density in the subsequent pinch, while also contributing to reproducibility by providing a "fixed frame" at the breakdown surface from which a flux of runaway electrons can originate. A corroborating study by Zakaullah et al.[8] demonstrates that limited insulator conditioning and shot history can enhance yield through local conductive zones, but that excess conditioning quenches yield altogether. Though these papers show that surface conditioning plays a significant role in the initiation of the current sheath, limited research has followed.

Theory underlying surface effects

Breakdown has a significant impact on the pinch. More recent studies presented by Yordanov et al. on the topic of breakdown in a DPF suggest an anisotropic electron-energy distribution function more accurately describes the breakdown evolution[14,15]. Using Monte Carlo simulations the electron energy distribution function is characterized throughout the breakdown phase which exhibits an anomalous number of high energy (>100 eV) and low energy (<10 eV) electrons. This suggests, when compared with simulations based on a Maxwellian electron energy distribution, the breakdown would progress at a faster rate due to the high energy electrons but that the real ionization rate should be lower[16,17]. Yordanov points out that because experimentally characterizing the breakdown is challenging the development of these codes and

their accurate description of the breakdown is critically valuable in advancing this science. Feugeas et al. found that a higher current density in sheath formation resulted in a more intense pinch[18]. Donges et al. concluded 1) the space charge available to form a sheath depended on the pressure of the fill gas and 2) the formation of a sheath without filamentary structures was needed to maintain a single homogeneous plasma layer in the run down phase. This is an essential condition for a focused plasma with high energy density[19]. Krompholz et al. observed the formation of the plasma sheath strongly influenced the state of the final pinch. A knife edge prevented filament development in the breakdown and was observed to increase the neutron and hard X-ray yield by 20 and 100 percent respectively. Of note, the knife edge improved consistency of performance in neutron and X-ray yield[20]. All these substantiate the idea that the final pinch conditions and yield correlate to initial plasma sheath quality at the insulator.

One way to describe insulator breakdown is to characterize the ionization of constituents at the insulator surface and how they drift in the electric field[21]. The Townsend ionization coefficient can be interpreted as the average number of ionizing collisions an electron can initiate while traveling a unit distance. This coefficient,

$$\propto = Ape^{-\frac{Bp}{E}},$$

is described in terms of the pressure (p) of the fill gas in torr and the electric field strength (E). Here the constants A and B are dictated by the conditions of the breakdown. Additionally the drift velocity of a weakly ionized gas can be described as

$$V_e = \frac{e}{m} v_{ea} E$$

and e, m, and v_{ea} are the electron charge, mass and ionization collision frequency with atoms respectively. Additionally, the present charge will affect the electric field as described by Poisson's equation,

$$\nabla \cdot \mathbf{E} = -\frac{4\pi}{\varepsilon} e(n_i - n_e),$$

which will couple the conservation equations describing persistence of electrons ions and excited states of neutral atoms,

$$\frac{\partial n_e}{\partial t} + \nabla \cdot (n_e \mathbf{V}_e) = Q_e^+ + Q_e^- + D_e \nabla^2 n_e,$$

$$\frac{\partial n_i}{\partial t} + \nabla \cdot (n_i \mathbf{V}_i) = Q_i^+ + Q_i^- + D_i \nabla^2 n_i,$$

and

$$\frac{\partial n_*}{\partial t} = Q_*^+ + Q_*^- + D_* \nabla^2 n_*$$

where n, $\mathbf{V}$, D, Q^+, and Q^- are defined as the density of particles, the drift velocity vector, the diffusion coefficient, the number of particles produced per unit volume and unit time, and the number of particles lost respectively. Using this description the electric fields generated between the anode and cathodes in a DPF are strongest for an optimized pressure[21].

This implies for each DPF system there is an optimum pressure for uniformity and timing of insulator breakdown, which is important because the breakdown influences the pinch conditions and thus X-ray yield [18,19,20]. Additionally, it suggests that there is an optimal ionization density in the region of the insulator when considering yields from the pinch. This idea is corroborated in Zakaullah and colleagues' work where increases in neutron yield and

improved sheath formation were observed when a beta radiation source was positioned near the insulator[22]. The source, by ionization of the fill gas, will influence the population and azimuthal density distribution of electrons available to begin the cascade at the onset of the breakdown. It is worth noting their observation that neutron yield is optimized with various pressure and activity combinations and that, when optimized, further increasing the source activity can notably reduce the neutron production in deuterium filled DPFs.

Plasma effects on optical backlights for diagnostic purposes

Plasmas can exhibit a wide range of responses to optical probing dependent on the state of the plasma. Factors include electron density, temperature, and fluctuations of the plasma as well as the parameters of the laser (intensity, wavelength, modulation, etc.).

Electron density effects

When sufficiently dense, plasmas can reflect electromagnetic waves. For free electrons in a plasma, assuming the simplified geometry presented in Figure 2, the relevant equation of motion, for free electrons in a plasma, assuming the simplified geometry presented in Figure 2,

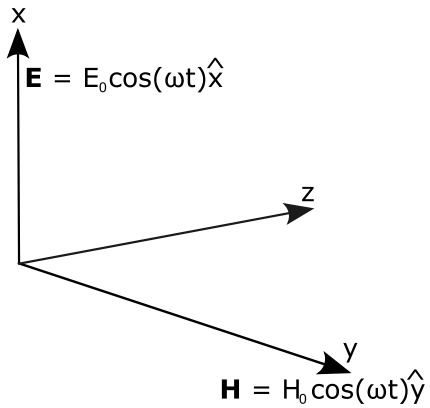

Figure 2. Simplified geometry for laser probing effects with E and H restricted to x and y coordinates[23].

the relevant equation of motion,

$$m_e \dot{v} = e\, E_0 \cos \omega t,$$

means that the free electron current,

$$j = n_e e v = n_e e\, \frac{eE_0}{m_e \omega} \sin \omega t,$$

and the displacement current,

$$\dot{D} = -\omega \epsilon_0 E_0 \sin \omega t$$

exhibit opposite phase. Taking the x component of Ampere's law,

$$\boldsymbol{\nabla} \times \mathbf{H} = \dot{\mathbf{D}} + \mathbf{j},$$

the relative permeability of the free electrons is known with

$$\left(1 + \frac{j}{\dot{D}}\right) \dot{D} = \epsilon_r \dot{D}.$$

For the electromagnetic wave in glass the relative permeability dictates the speed of the wave,

$$v = \frac{1}{\sqrt{\epsilon_r \epsilon_0 \mu_0}},$$

which means the index of refraction can be defined in terms of the relative permeability,

$$n_{ref} = \frac{c}{v} = \sqrt{\epsilon_r}.$$

So in this simplified case of the plasma, knowing the relative permeability is to know the index of refraction,

$$n_{ref} = \left(1 + \frac{j}{\dot{D}}\right)^{1/2} = \left(1 + \frac{\frac{n_e e^2 E_0}{m_e \omega} \sin \omega t}{-\omega \epsilon_0 E_0 \sin \omega t}\right)^{1/2} = \left(1 - \frac{{\omega_p}^2}{\omega^2}\right)^{1/2}.$$

With the critical density, n_{cr}, defined by the condition, $\omega_p = \omega$, the plasma index of refraction, n_{ref}; the electron density, n_e; and the critical density are related by

$$n_{ref} = \sqrt{1 - \frac{n_e}{n_{cr}}}$$

where $n_{cr} = 1.1 \times 10^{21} \lambda^{-2} [\mathrm{cm}^{-3}]$ and the wavelength, λ, is in μm. The number of fringe shifts N observed in the interferometer would then be

$$N_f = \frac{\delta\phi}{2\pi} = \frac{1}{\lambda} \int_0^L \left(1 - n_{ref}\right) dl \approx \frac{n_e}{2n_{cr}} \frac{L}{\lambda}$$

with the ray trajectory along the path of the integral where *dl* is the differential path length and *L* is the path length through the plasma[24]. The effect of refraction here is neglected.

When the electron density is low enough the probing light can undergo a phase shift,

$$\delta\phi = \frac{n_e}{2n_{cr}} \left(\frac{L}{L_T}\right)$$

where L_T is the wavelength of the transmitted, phase-shifted ray,

$$L_T = n_e \frac{\delta z}{\delta n_e}$$

n_e, n_{cr}, and L_T are the electron density, critical density, and the wavelength of the incident ray (see Figure 3). The shift in phase drives the fringe shifts in the interferometer and infers the electron density of the plasma.

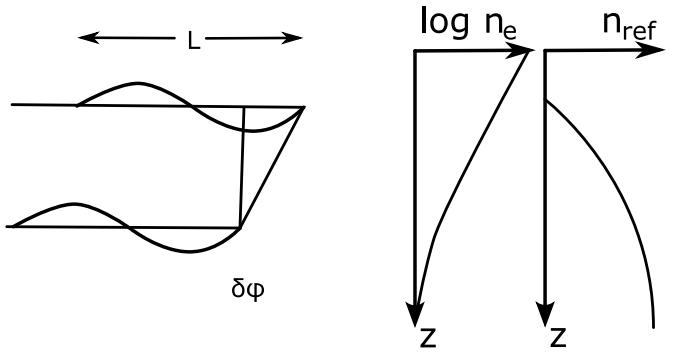

Figure 3. Phase shift of light incident on a plasma. Phase elongation shows a redirection of the wavefront indicating a bending of light (left). Electron density being probed (center) and the associated index of refraction (right)[23].

This shift in phase will bend the light as seen in the wave fronts arriving at the same point in space at different times. This results in deflection of the light passing through a plasma and is the principle behind schlieren imaging where, in the case of an optical probing setup, the deflected light passes around the stop and creates an image in the camera.

Research Objectives

From the aforementioned literature studying the role of the insulator in successful DPF operation, it is clear that the insulator has a profound effect not only the breakdown and formation of the plasma sheath, but also an effect on the delivery of current to the pinch via mitigating leakage current. Almost all insulator materials employed in prior literature will either have been cut or machined to fit the DPF in question, potentially introducing micro-scale irregularities to the insulator structure exposed between the electrodes. To this end, the research detailed here is designed to investigate, for a fixed insulator material, how modifications to the structure of an insulator surface can influence the dynamics and X-ray production for a Ne filled DPF. Chapter 2 gives a detailed description of the experimental setup and diagnostics employed. Chapter 3 describes optimization of the DPF in order to establish a baseline for operation and

yield, while Chapter 4 compares the effects of insulator surface conditioning, with particular emphasis on sheath initiation, pinch uniformity, and X-ray production. Chapter 5 reports the main conclusions of this work and recommendations for future work.

Chapter 2 Dense Plasma Focus at UCSD

Experimental Setup

10 kJ DPF Design

Our requirements were to design and build a 10kJ Mather type DPF at University of California, San Diego. The capacitor available to build the system was an Aerovox 20.7 μF capacitor rated for 50 kV with a 40 nH estimated stray inductance. In a capacitor electrical energy=1/2 cV^2 and because the energy end point and the capacitance are known the required voltage can be calculated for the 10 kJ DPF as 32 kV. Since V=IR the peak current of the system can be calculated by substituting $L/C^{1/2}$ for R. Knowing the inductance, capacitance, and the voltage we can calculate the peak current as 450 kA. The capacitor was charged to 21 kV in the present experiments (~4.4 kJ stored energy). The circuit inductance is 110 nH, resulting in a 2.2 μs current rise time and a peak current of 250 kA.

The electrode configuration is shown in Figure 4 and Figure 5(a). The anode and cathode are made of copper and are separated electrically by a PTFE cylinder (yellow in Figure 5(a)) which accepts an interchangeable exposed insulator (gray). In this work the interchangeable insulator is made of borosilicate glass with an outer and inner diameter of 1.75" and 1.5" respectively and a height of 1.625". The portion of the insulator exposed above the cathode deck in the vacuum chamber is 1.125". The borosilicate insulators are installed with high gloss as-manufactured (cast or drawn) finish, henceforth referred to as the smooth insulator, or with one of several surface patterns as described in chapter 4. The DPF chamber is prepared for each series of shots by evacuating the vacuum chamber to below 10^{-4} torr before backfilling with neon gas to the desired fill pressure.

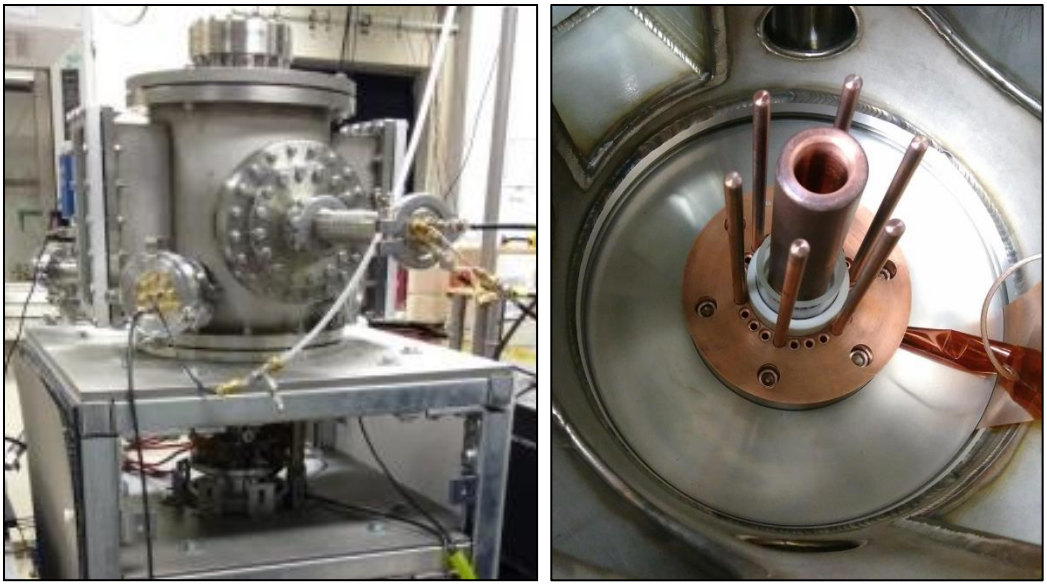

Figure 4. Dense Plasma Focus at UC San Diego, capacitor not shown but located below, switch visible on lower deck and vacuum chamber visible on top deck (left). Top view of vacuum chamber interior showing electrodes and insulator installed (right).

Lee Model for electrode dimensions

The Lee model can be used to find the dimensions of the electrodes for a design optimized for energy coupling. The goal is to time the pinch of the sheath in the DPF with the peak current. Peak current is dictated by the electrical characteristics of the system, which gives the rise time of the circuitry of the system, and the timing of the sheath pinch is dictated by the dimensions of the electrodes. This is because in a general sense, DPFs have a constant drive parameter—the speed of the sheath in the coaxial voids between the electrodes is generally the same for any DPF[25].

A drive parameter for the system, 77-89 kA/cm mbar$^{1/2}$ was taken from above cited the Lee paper[25]. This allows a calculation to predict what the optimal anode radius should be because the drive parameter is defined as the current/anode radius x pressure$^{1/2}$. An assumption about pressure is also necessary; our assumption for the ideal pressure for neutron yield is 6 mbar of

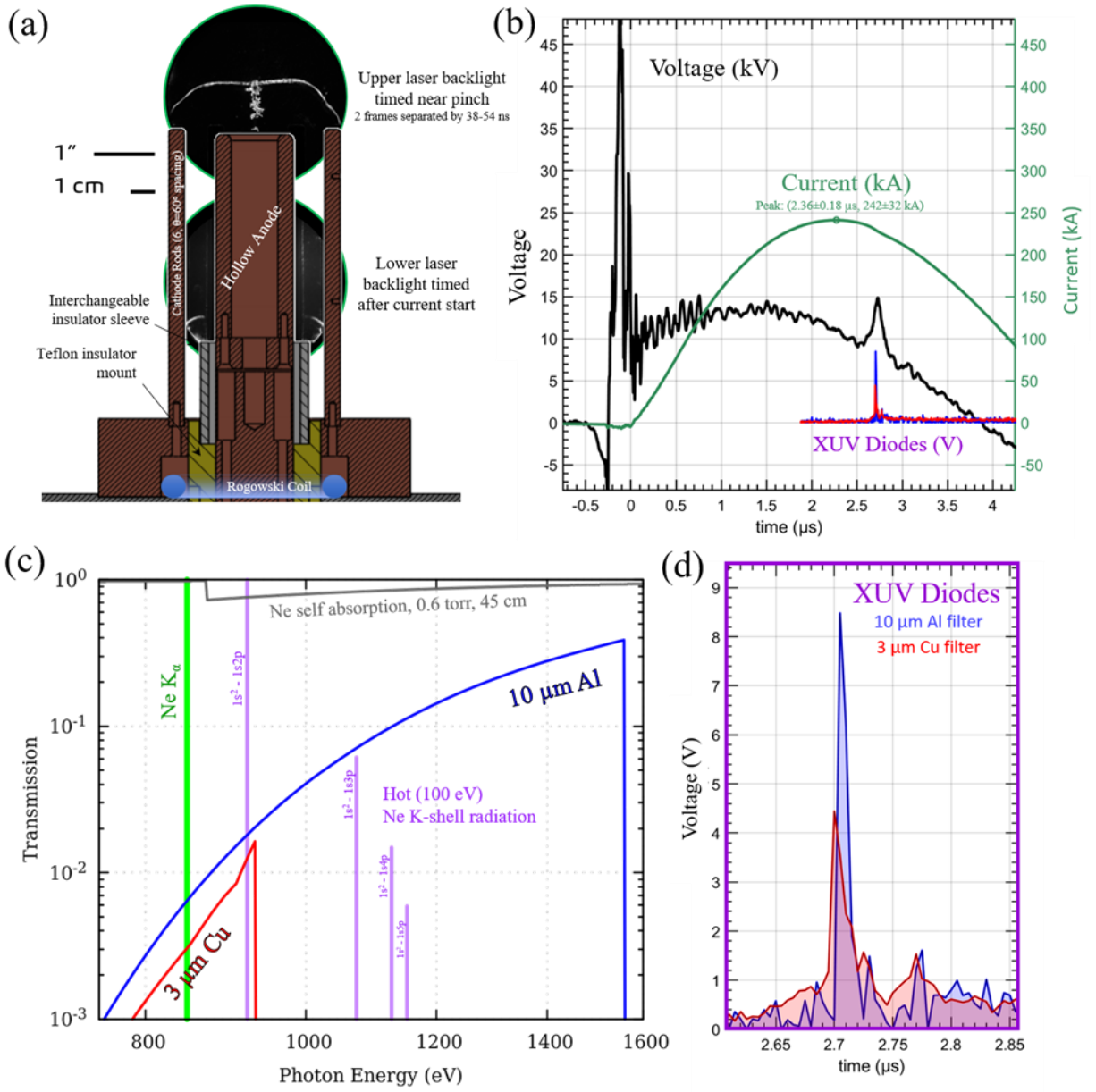

Figure 5. (a) DPF electrode and insulator geometry. The anode (center hollow copper electrode), cathode (series of six equally spaced copper rods) and borosilicate insulator (grey) allow quick changes of components without system disassembly. The insulator is installed into a Teflon separator (yellow) which provides electrical isolation of the pulse line from the grounded vacuum chamber. X-ray sensitive photodiodes are positioned to view the pinch region while optical probing illuminates the pinch and breakdown regions (black circles) to allow schlieren/interferometer imaging. (b) Characteristic current and voltage signatures of the DPF at 4.4 kJ operation as measured at the base of the anode inside the chamber and at the power feed as it enters the chamber respectively. The blue and red traces are 10 µm Al and 3 µm Cu filtered X-ray photodiode signals respectively showing the timing of the pinch in relation to the current and voltage evolution of the system. (c) Filter transmission of the 10 µm aluminum and 3 µm copper foils (blue and red respectively) overlayed with expected K-shell radiation from a T_e = 100 eV Ne plasma (Ne IX lines). Both filters transmit the neon K_α line at 848.6 eV, but the copper filter blocks X-rays above 929.7 eV and the aluminum filters X-rays above 1557 eV. Self-absorption of the Ne fill gas (gray line) is marginal in the range of operating pressures at a distance of 45 cm. (d) Magnified photodiode signals.

deuterium filled gas. The optimized anode radius for our system was calculated at approximately 3.15 cm.

Multi-Gap Multi-Channel Switch

Our system required a switch that can withstand 500 kA while keeping a low inductance (<50 nH). There were three iterations of the switch design. Currently the switch consists of two steel endplates fitted with brass annular electrodes on the interior, separated by an acrylic cylinder that encases the switch. Inside the acrylic cylinder are mounted two rings that each hold an array of twelve azimuthally evenly spaced brass electrodes. The switch is triggered by feeding a voltage pulse directly into the course of electrodes held by the top brass ring. The acrylic housing allows the air pressure to be controlled inside the switch which tunes the breakdown to the desired voltage.

With use, plasmas from the electrodes erode the pins that hold the electrodes in place. On the order of ~100 shots those pins begin to fail causing the electrodes to fall one by one to the bottom of the switch. This changes the number of channels in the switch that close thereby influencing the inductance. This poses a challenge to reproducible performance of the DPF system, particularly leading to variations in the peak current and timing. Refurbishing the switch involves realignment of the entire system which is time-intensive. Future improvements to switch design could mitigate these challenges.

DPF System Circuitry Characterization

A 21 kV capacitor voltage results in a peak current of 242±32 kA, with a 2.36±0.18 μs rise time (the uncertainty represents the standard deviation of the measurements over all shots

taken). The voltage and current data are digitally collected on a 16 channel 2-GS/s Tektronix TLS 216 oscilloscope, from the voltage divider positioned at the main power feed between the switch and the vacuum chamber and from the pair of Rogowski coils, one positioned at the output of the capacitor and one at the base of the anode inside the vacuum chamber. A representative current and voltage trace measured at the anode base are shown in Figure 5(b). Current traces for a series of 15 consecutive shots are represented in Figure 6. Due to electromagnetic noise at the onset of breakdown, the current (I) start times are calculated by extrapolating a linear fit of the current trace between 10 and 20% I_{max} to the current start (I = 0). Several iterations of this calculation were tested including changing the range of trace used and fitting of the data to non-linear functions; taken together these calculations of the current start time suggest an approximate confidence interval on the order of ±20 ns. All timings presented henceforth are with respect to the current start time (unless noted otherwise) and will inherit this uncertainty.

Table 1. Lee Model Parameters for the 10 kJ dense plasma focus at UCSD.

Capacitance	C_0 (μF)	20
Static inductance	L_0 (nH)	110
Circuit resistance	r_0 (mΩ)	6
Cathode radius	b (cm)	5.715
Anode radius	a (cm)	3.15
Anode length	z_0 (cm)	11.5
Charging voltage	V_0 (kV)	21
Fill gas pressure	P_0 (torr)	0.5
Fill gas molecular weight	MW	20
Atomic number of the gas	A	10
Axial mass swept-up factor	fm	0.07
Axial current factor	fc	0.65
Radial mass swept-up factor	fmr	0.18
Radial current factor	fcr	0.65

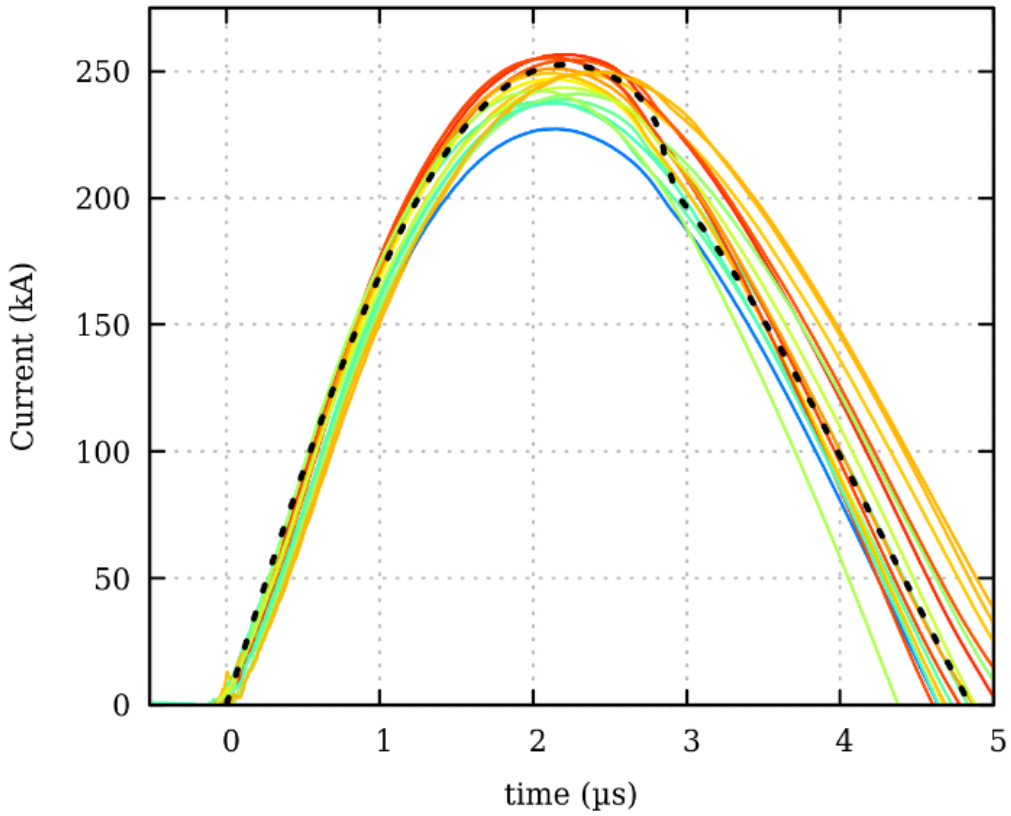

Figure 6. Current traces for 15 consecutive shots using 0.5 torr Ne fill gas. Each trace is colored based on the maximum current for that shot (red for higher and blue for lower max currents). The black dashed line is the current calculated using the Lee model.

Representative current traces (from the Rogowski coil located at the anode base) at 0.5 torr fill pressure were used to fit the Lee Model code[25] (version RADPFV5.15de.c1) to obtain order of magnitude predictions of the plasma sheath dynamics, pinch ion density (n_i), and temperature (T). Table 1 details the model parameters. The peak axial and radial sheath velocities are predicted to be 70 km/s and 225 km/s respectively. The modeled ion density n_i and plasma temperature T at the pinch are on the order of 10^{17} cm^{-3} and 100-200 eV, with an expected pinch duration of 31 ns occurring at 2.85 μs and producing 10 J of line radiation over 4π steradians.

Diagnostics

The objective of this project is to collect comprehensive data sets on a wide array of diagnostics for each shot. This would enable correlation of features in the data without the complication of shot-to-shot variation. The main plasma diagnostic suite for these experiments includes: a voltage divider to measure the voltage throughout the shot; Rogowski coils to measure current; filtered photodiodes to capture soft X-ray emissions; a wide range visible spectrometer; and two Mach Zehnder interferometers for optical laser probing of the insulator region and the pinch region during the same shot. Furthermore, the pinch region interferometer has a polarized separator that allows for two images to be taken in the same shot separated by <100 ns and can be quickly configured for schlieren imaging and shadowgraphy.

Main Power Feed Voltage

To characterize the voltage of our system we installed an array of resistors from the main power feed to the anode of the DPF chamber. The array is terminated with a 50 ohm resistor to the frame allowing for a voltage divider that can be used to measure in a proportionate way the voltage of the anode during operation. The voltage divided by the resistor array and 50 ohm resistor is fed into a 16 channel Techtronix scope and the signal is proportionate to the voltage at the anode within the frequency response of the voltage divider system. Characteristic voltage traces of our system are shown in Figure 5(b).

One of the limitations of this diagnostic is the physical durability. Leads of the resistors used in the array are very delicate and fragile and have failed due to mechanical stresses multiple times to date. To rectify this issue it is recommended that a stackable high power resistor array be used in the future. Additionally, since the voltage divider spans the main power feed and the

grounded frame it provides a higher probability of unwanted breakdown resulting in current losses in the pinch and possible damage to components. While this unwanted breakdown has not happened along the voltage divider it is a concern.

Another way to diagnose the voltage at the main power feed would be to install a D-dot monitor.[26] The advantage of D-dots is that they remotely sense the voltage with minimal effect on the system. The only potential effect on the system would be a negligible change of capacitance to the power feed. Calibration of D-dots would require the temporary use of a voltage divider.

Main Power Feed Current

Characterizing the current of the main power feed for the system required building and installing Rogowski coils. Two coils were built and installed in the system, one at the output of the capacitor and the second at the base of the anode inside the vacuum chamber. The coil was fabricated beginning with a BNC terminated RG232 coaxial cable. To make the capacitor output viewing coil the unfinished end of the RG232 cable was stripped of its cladding down to the dielectric core that surrounds the central conductor. Then that dielectric core was wrapped with copper wire with three rotations per centimeter of dielectric core length. The wrapped wire was soldered to the central conductor on the unfinished end and then to the coaxial conductive cladding on the other end. This was then wrapped with Kapton tape for insulation and then wrapped in alternating layers of copper tape and Katon tape such that the copper tape did not come back in contact with itself. This reduces the noise of stray magnetic fields not associated with the main power feed current. For the vacuum chamber coil fabrication a similar method was employed, using a smaller coaxial cable made with vacuum acceptable materials. Instead of

using Kapton tape as an insulator the coil was slipped into a vacuum acceptable insulating sleeve. It was shielded from the plasma environment under the cathode plate of the system. The capacitor output Rogowski coil was calibrated using a NIST-traceable current viewing resistor to determine the calibration factor. The vacuum chamber coil was cross-calibrated against the first coil.

These coils have been largely problem free and seem to respond well to the system. B-dots were not used for this application since they would provide only localized magnetic field measurements as opposed to the holistic field measurements provided by the Rogowski coil. Due to this the Rogowski coils are a superior choice to B-dots.

Filtered Photodiodes

The time-resolved X-ray emission was captured using two Si PIN photodiodes (Opto Diode p/n AXUV20HS1) biased at -150 V, filtered with either 10 μm thick Al or 3 μm thick Cu and located 45 cm away from the central axis of the machine. These two filters provide sensitivity to the cold Ne K-shell radiation (K_α =848.6 eV) and hot K-shell radiation (922.0-1164.9 eV, with estimated relative magnitudes calculated via the NIST Atomic Spectra Database[27,28] for Saha-LTE spectrum with electron temperature and density of 100 eV and 10^{17} cm^{-3} , see Figure 5(c)). Transmission curves for the selected filters and the simulated X-ray spectrum are shown in Figure 5(c). The simulated spectrum was normalized to the $1s^2$-1s2p line and the K_α is given a nominal intensity of 1 for illustrative purposes. Also shown in Figure 5(c) is the expected self-absorption of the Ne fill gas at 0.5 torr at a distance of 45 cm. All transmission curve data was sourced from Henke et al.[29] Characteristic diode signals are shown in Figure 5(b) and (d). Cross-calibration of the photodiodes showed a response difference less than 2% as

measured by 10 shots with both diodes filtered by 10 μm Al. The selected filters will capture different components of the expected radiation and are used to compare shot-to-shot variation rather than provide an absolute measure of X-ray yield for the system.

Spectrometry

An Ava Spect spectrometer, a wide-range spectrometer that covers from 300-850nm, is set up to acquire visible plasma self-emissions from the insulator surface and breakdown region. This provides a description of the contaminants in the Ne gas at the insulator surface.

Optical Laser Probing

Interferometry is an important diagnostic because the phase shift observed in the fringe map infers the electron density of the plasma being probed. This gives not a single number, but rather a 2D map of the phase shift. When an image is captured from the interferometer without any plasma present, simply capturing the native interference within the interferometer itself, an interference pattern is observed at the detector (in this case a Canon Rebel T6 camera). This generates a 2D map of the fringes created by the interference. This interference pattern is called the reference image, having no plasma influence. During a shot there is plasma in the probing beam of the interferometer. The presence of the plasma shifts the phase of the probing beam (see Chapter 1, Figure 3). This will generate a different interference pattern at the camera. In other words, the presence of the plasma results in a movement of the fringes when compared to the reference image. The movement of those fringes infers the density of the plasma and through post-processing a 2D areal density map can be constructed. The advantage of this type of interferometry is that an entire map of plasma density information is created, not just a single number. This can also provide structural information about the plasma, not just its density.

Schlieren imaging is made possible because the shift in phase equates to a shift in the wave front of the electromagnetic wave so the wave front is no longer orthogonal to the k vector. This means the light from the laser is bent by the plasma, and the ray will no longer be blocked by the schlieren stop and will pass through to the camera, thus generating a schlieren image.

The optical laser probing of both the pinch and the insulator regions are timed to capture snapshots of the plasma sheath in the early run-down and the pinch phases within a single shot. Two Nd:YAG lasers (EKSPLA NL301G and Quantel BigSky), frequency doubled at λ=532 nm with 10 ns FWHM pulses and 75mm beam diameter, were used to backlight both the upper and lower regions of interest, providing spatially-resolved images of the plasma. The probed regions are shown in Figure 5(a). The images from both probing systems are captured with Canon Rebel T6 digital cameras and have a 25 μm resolution.

The upper laser probing system allows either schlieren imaging or Mach-Zehnder interferometry of the pinch region with two frames separated in time; in these experiments the frame separation was set to either 39 or 50 ns by changing the delay line path length. (With the addition of a handful of optics and two more cameras it would be possible to capture both interferometry and schlieren images simultaneously at two points in time of the shot.) The advantage of two pictures in a single shot is the ability to capture the evolution of the plasma, allowing dynamic information about the plasma to be obtained. The lower laser probing system is configured for simultaneous schlieren imaging and Mach-Zehnder interferometry at a single time for each shot. With appropriate timing this allows simultaneous schlieren and interferometry capture of the plasma sheath during the early to mid run-down phase. Coupled with the imaging from the upper laser probing system, one can begin to correlate features

observed in the run down phase with features observed at two points in time in the pinch phase, all without the complication of shot to shot variation.

Chapter 3 Pinch Dynamics and Performance

Neon Pressure Optimization for X-ray Yield

This chapter contains a characterization of the DPF system. In particular, how the X-ray performance depends upon Ne fill gas pressure when employing a smooth borosilicate insulator (similar to these studies[30,31,32]). The experimental yield data collected is plotted in Figure 7. When fitting Gaussian curves to the mean and maximum values observed in yield data the optimal pressure for this system is predicted to be just under 0.6 torr with a yield of ~0.24 J. The single shot maximum in this study was observed at 0.6 torr Ne fill pressure with a yield of 1.26 J which agrees with literature on X-ray yield of similar scaled Ne-filled DPF[30]. Figure 7 details each measurement of the background-subtracted time-integrated photodiode signal (units of Vμs) above the calculated X-ray yield over 4π (units of Joules).

The data plotted in the lower panel of Figure 7 accounts for the relative integrated signal of both the Al- and Cu-filtered diodes, responsivity (amps/watt) of the diode, 20 mm^2 diode area, 45 cm distance from the pinch, average X-ray attenuation via self-absorption from the neutral Ne fill gas at varying pressure, and transmission curves averaged proportionally to the expected strength of the K-shell radiation (i.e. subtracting the signal of the Cu filtered diode subtracted from the Al filtered diode).

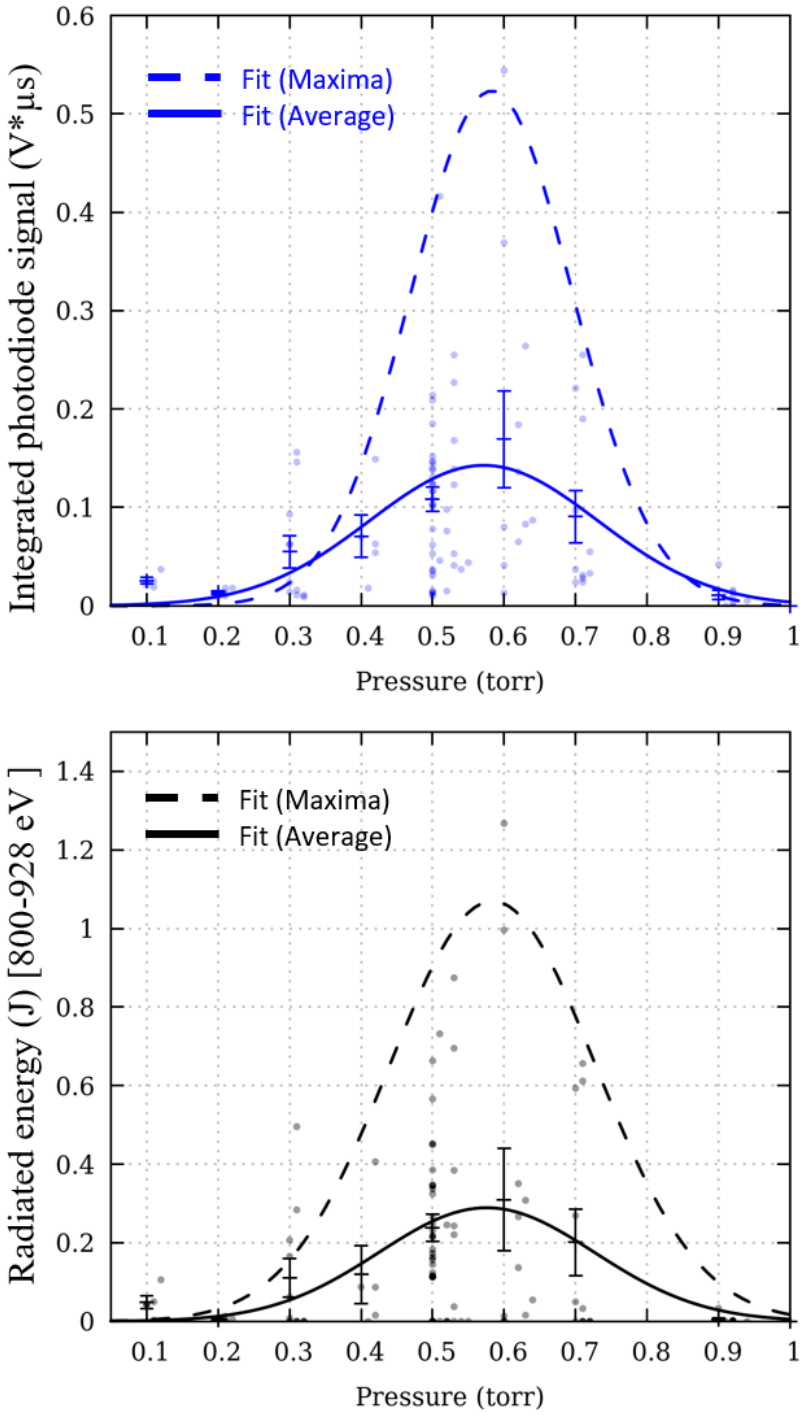

Figure 7. Experimental x-ray yield observed at various pressures and averages plotted with standard deviations as errors. Both average yield (solid line) and maximum yield (dashed line) peak at ~0.58 torr Ne fill gas for (top) Integrated voltage signal from Al filtered diode; (bottom) Ne K-shell X-ray yield (J) calculated by subtracting the Cu filtered signal from the Al filtered signal after taking account for the necessary corrections noted in the main text..

Pictoral Current Sheath Data

To provide a comprehensive view of the plasma evolution in this system, three compilation figures are included: Figure 8, a complete imaging analysis for one shot; Figure 9, an album comprised of multiple shots taken with varying laser backlight timing to illustrate the dynamics and common features of the plasma sheath from the end of the radial phase throughout the lifetime of the pinch and showing plasma remnants remaining after peak compression; and Figure 10, a comparison of the pinch structures as described by schlieren imaging near the time peak X-ray signal is observed as a function of pressure.

Density Analysis

Figure 8 shows a combination of schlieren images and interferograms measured with respect to the timing of the peak X-ray signal ($t_{X\text{-}ray}$) for the pinch region and as a fraction of the peak current (I_{peak}). Schlieren imaging yields a better representation of small-scale plasma structure than density maps from interferometry analysis. However, the sheath in this system is often difficult to detect in the breakdown region using schlieren methods when within 1-2 cm of the insulator. Presumably, this is due to the low electron density of the plasma sheath while in the breakdown and lift-off phases. Interferometery methods are better suited to image sheath liftoff and initial propagation because they are more sensitive to lower density plasmas. For this reason, we rely upon interferometry analysis to gain both quantitative and qualitative information regarding the position and structure of the plasma sheath in the breakdown region, using the open source Neutrino image analysis code.

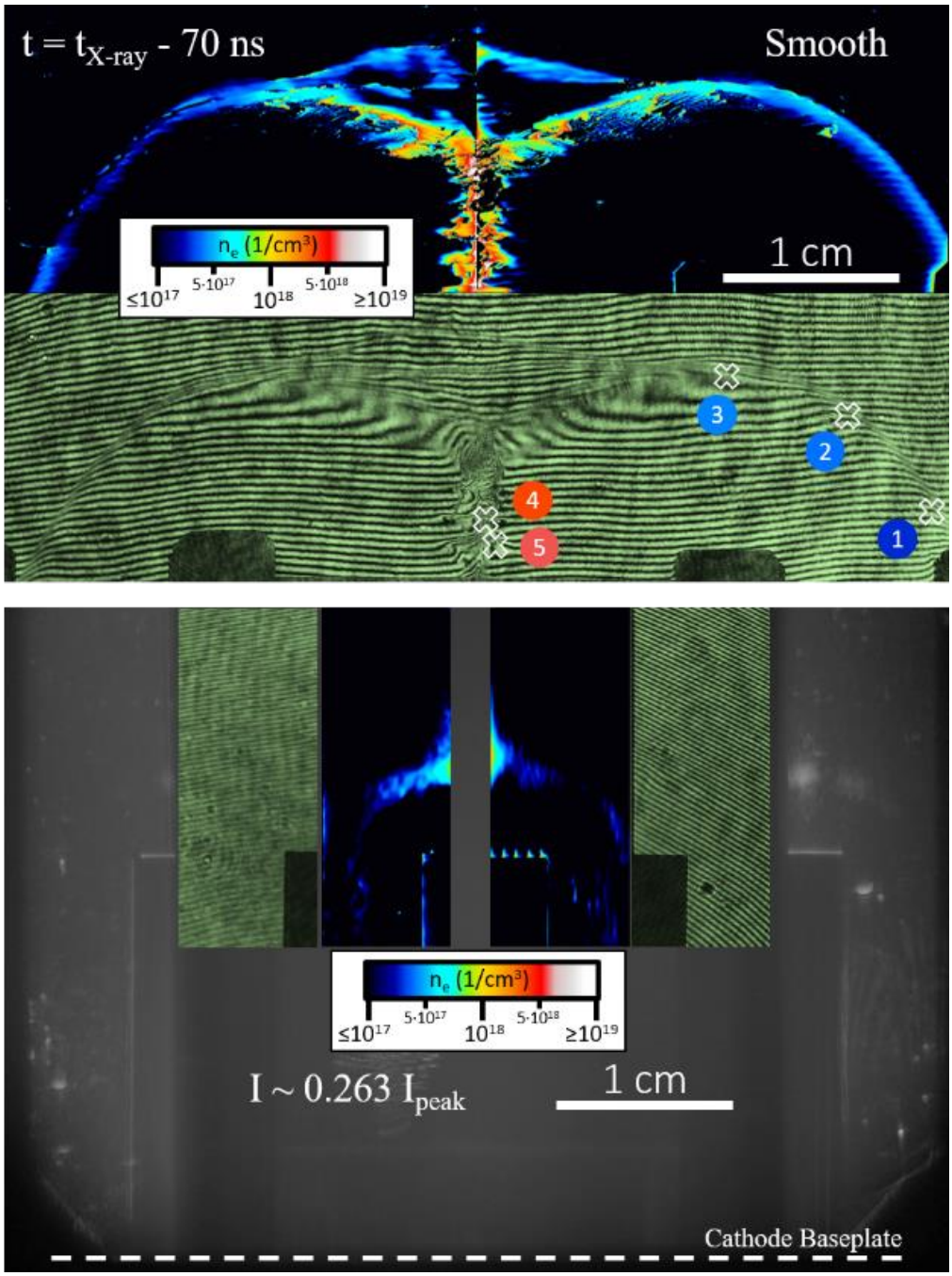

Figure 8. Set of laser backlit images from a single shot (with smooth insulator sleeve). The top panel displays the raw fringe field from the pinch region viewing interferometer (grayscale with green tint) and resulting density map (false color image) while the bottom panel shows schlieren (grayscale) with inlays of corresponding interferometer fringe field (grayscale with green tint) and density field interferogram (false color image). All images in this figure have the same spatial scale but the inlaid images in the lower panel have been shifted toward the axis to allow viewing of the corresponding region near the top of the insulator. Raw data fringes are shown in grayscale with green tint overlay (for legibility of labels) while schlieren images are displayed in standard grayscale. Analyzed interferograms are colored on a log scale according to their electron density (with units of cm-3). Points selected for density analysis are marked by white X's and color-coded according to the scale presented in the false color density map. Density values resulting from these estimates are given in Table 2.

Table 2. Electron densities (ne) calculated from interferograms in Figure 8, a characteristic shot featuring a smooth borosilicate insulator (lines 1-5) and an exterior horizontal grooved insulator (lines 6-10).

	Approximate description of location	Fringe calculation n_e (10^{17} cm^{-3})	Neutrino analysis n_e (10^{17} cm^{-3})
1.	Sheath connection to cathode	1.4	3.2
2.	¼ of the arc from cathode to pinch	2.4	3.3
3.	½ of the arc from cathode to pinch	3.8	4.8
4.	First Pinch location	40.3	28
5.	Second Pinch location	56.4	33
6.	Sheath connection to cathode	1.9	3.4
7.	¼ of the arc from cathode to pinch	3.3	5.4
8.	First Pinch location	16.1	29
9.	Second Pinch location	16.1	36
10.	Third Pinch location	12.1	27

Abel inversion is used to convert the 2D-projected areal density map to a density map describing the spatial distribution of the electron density along a plane that dissects the 3D plasma structure. The plasmas observed in this system are complex and poorly described as cylindrically symmetric, but the interferometry post processing assumes cylindrically symmetric plasma to provide density estimates. This means the analysis may yield estimates that deviate from the actual densities. Additionally, the gradients in the neutral gas density driven by the snowplow action of the sheath also affect the observed phase shifts described by the interferometer fringe images.

Density values are estimated manually from the fringe shifts of the raw data. These are calculated by computing the difference in fringe counts between two corresponding points in both the fringe image from a shot (showing the influence of plasma on the fringes) and the reference fringe image with no plasma present but the same fill pressure. The first point is defined by where on a 2D bisecting plane the electron density value is desired (this will be in an area where the fringe field has been influenced by the plasma) and the second point is selected to

be at a location where no plasma influence or density perturbations are thought to exist in either of the fringe fields. The difference in fringe shift between these two points, when comparing the reference fringe field (interferogram with no plasma influence) and the probing fringe field (the interferogram with fringe shifts from the plasma) is scaled by a factor that takes into account the laser probing frequency and an integral inversion that requires estimates of the optical path length through the plasma volume at that location.

Neutrino analysis of the fringe images and these manually calculated estimates show disparities (from ~60-230%) but we estimate the accuracy of fringe inversion to be within a factor ~2. It is important to note that because the fringe image is a 2D projection of a complex and often multi-layered 3D plasma structure in phase space any one point in the Abel inverted density map cannot correspond only to a single point in the fringe image although estimates of the electron density corresponding to the specific locations in the density map can be constructed when considering the phase shift context presented in the fringe image. Quantitative electron densities at several positions (as noted in Figure 8) are compared to values calculated by the open source Neutrino code (Table 2).

Schlieren Imaging of the Pinch Region

The evolution illustrated in Figure 9 starting at 2.448 μs shows the plasma sheath as it completes the rundown phase and transitions to the radial phase. As the plasma sheath rounds the end of the anode, several periodic ripples can be observed on the trailing surface of the current sheath near the anode (2.448 and 2.457 μs) suggestive of Kelvin-Helmholtz instabilities noted in MHD simulations[33]. However, as the sheath expands beyond the cathode rods these instabilities fade and eventually are no longer visible. The sheath converges near axis by 2.683 μs and the

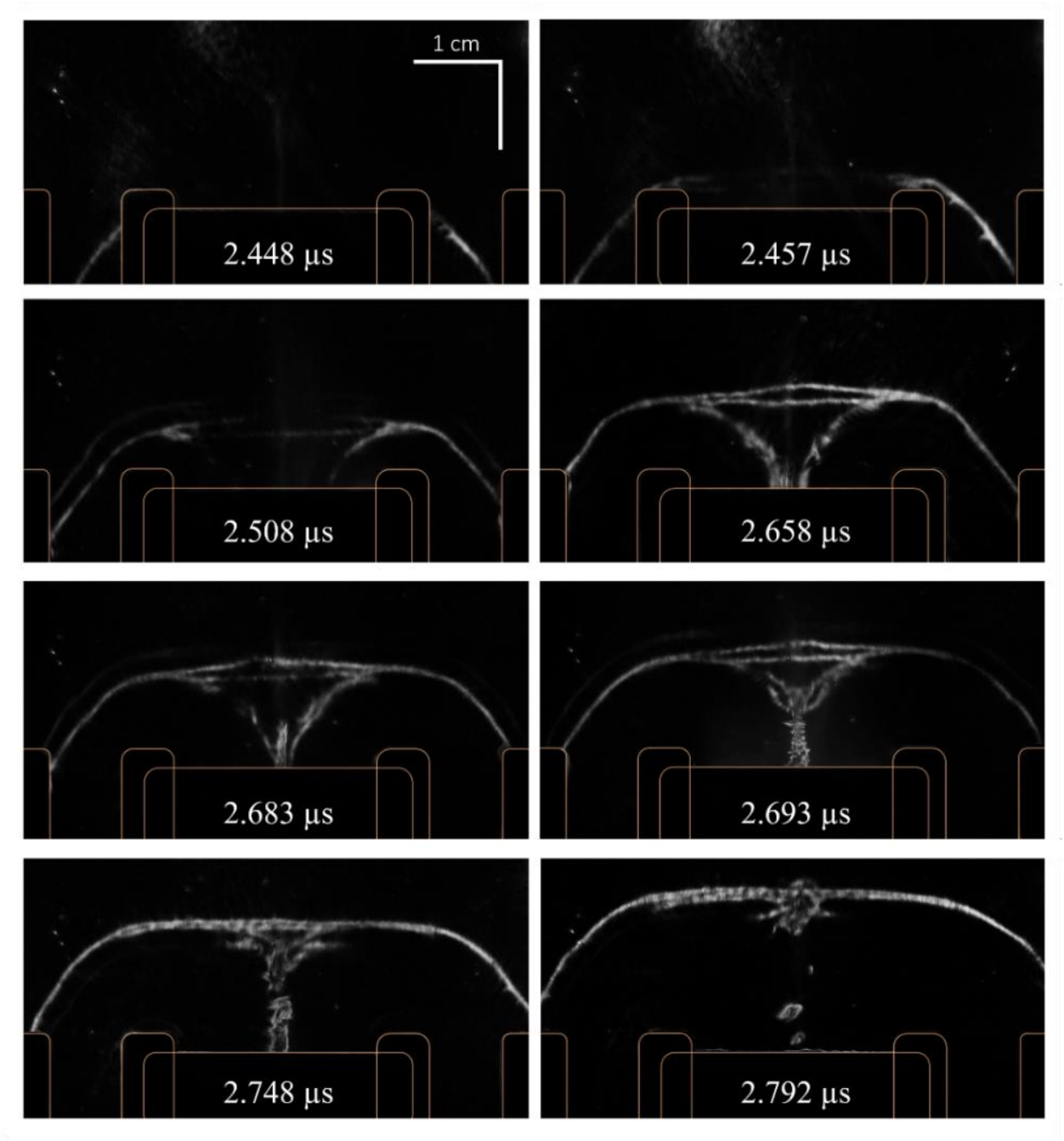

Figure 9. Compiled schlieren images album across multiple shots of the plasma evolution during the end of the axial rundown phase, radial collapse phase, pinch, and the beginning of the expansion phase all for neon fill gas at 0.5 torr. Projected outlines of the electrodes are shown as thin copper lines.

stagnation phase shows the development of instabilities at 2.693 and 2.748 µs. As convergence begins (2.683 µs), a bright area often arises apparently within the sheath. Speculatively, this could be a feature of preheating due to shock compression (causing a localized increase in

electron density) or possibly beam-target interactions, although literature suggests the beams develop in tandem with instability development. As the instabilities continue to grow the column breaks into plasmoid remnants (2.792 μs). It has been reported in literature that high electric fields develop during the disruption of the plasma column which may enhance acceleration of ions and electrons[34-35]. Typically, the pinched column persists for ~60 ns which is somewhat longer than the duration of the X-ray signal (measured to be on the order of ~10-20 ns FWHM) and column lifetime predicted by Lee model simulations (31 ns) of our system.

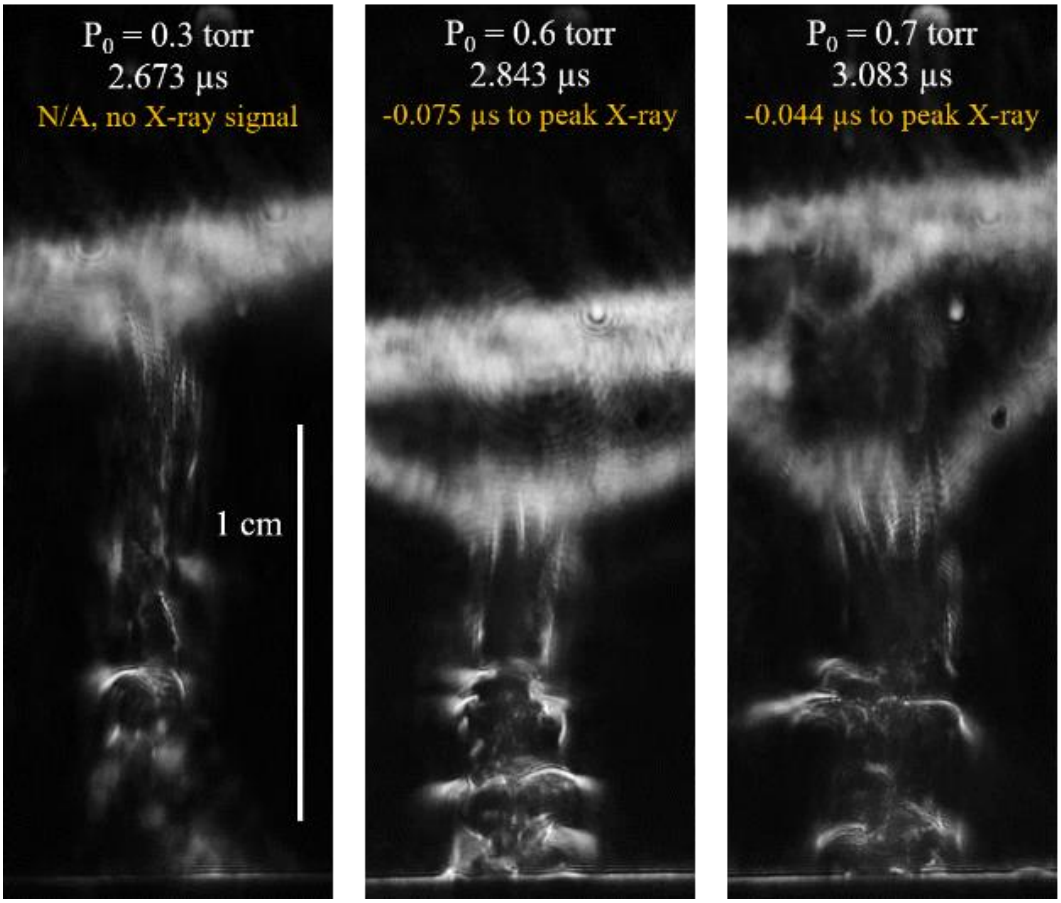

Figure 10. Characteristic pinch structures shown as monochromatic schlieren images for 0.3, 0.6 and 0.7 torr neon fill gas. Timings are given relative to the current start and peak X-ray signal (measured with a 10 μm Al filter).

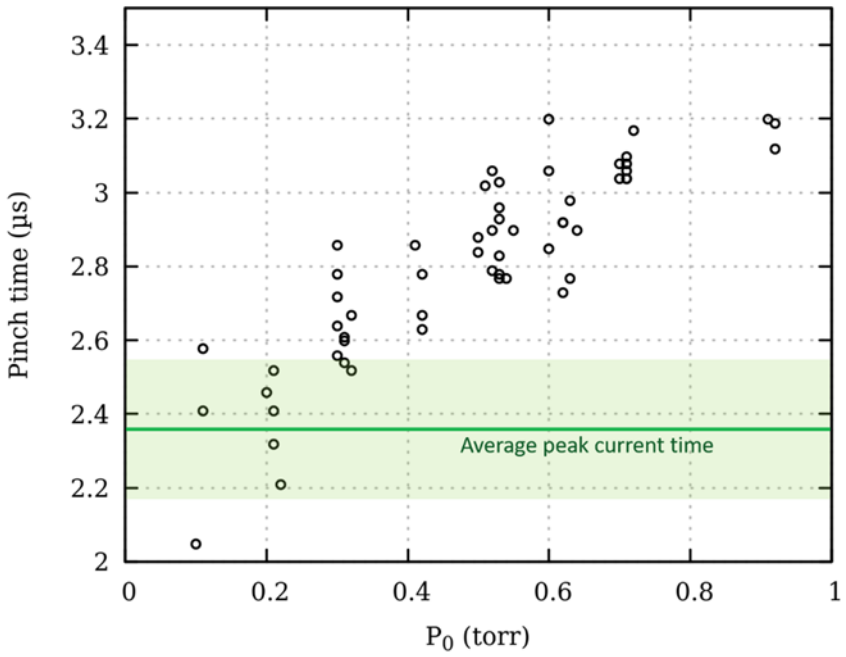

Figure 11. Characteristic pinch time as a function of Ne fill pressure. Average peak current and its deviation are shown as the solid green line and transparent green area.

Sheath Velocities

As shown in Figure 7, the pressure of the fill gas affects the X-ray yield. For instance a higher fill gas pressure results in a denser sheath, slowing the sheath axial velocity, which changes the timing of the pinch relative to the peak X-ray signal measured by photodiodes (Figure 11, with illustrative images of the pinches shown in Figure 10). This in turn affects X-ray yield due to the time dependence of energy coupling.

Essentially the pinch and the peak current must be timed to maximize the energy coupled to the load and maximize yield, i.e. under-massed pinches implode too early while over-massed pinches implode too late. The effective sheath velocity bears the largest influence on this timing. Velocities were calculated by measuring the relative sheath positions between the two frames of schlieren images timed near the end of the rundown phase (calculated sheath velocities shown in Figure 12, representative image shown earlier in Figure 9). Error bars represent the uncertainty in

the position of the leading edge of the sheath for these calculations. The smaller error bars between 0.5 to 0.6 torr are due to a smoother, narrower sheath at the end of the rundown phase at these pressures. A linear fit to the data is also shown in Figure 12: $v_{sheath\text{-}axial}$ = 59 km·s^{-1} -38 km·s^{-1}·torr^{-1} ·P_0.

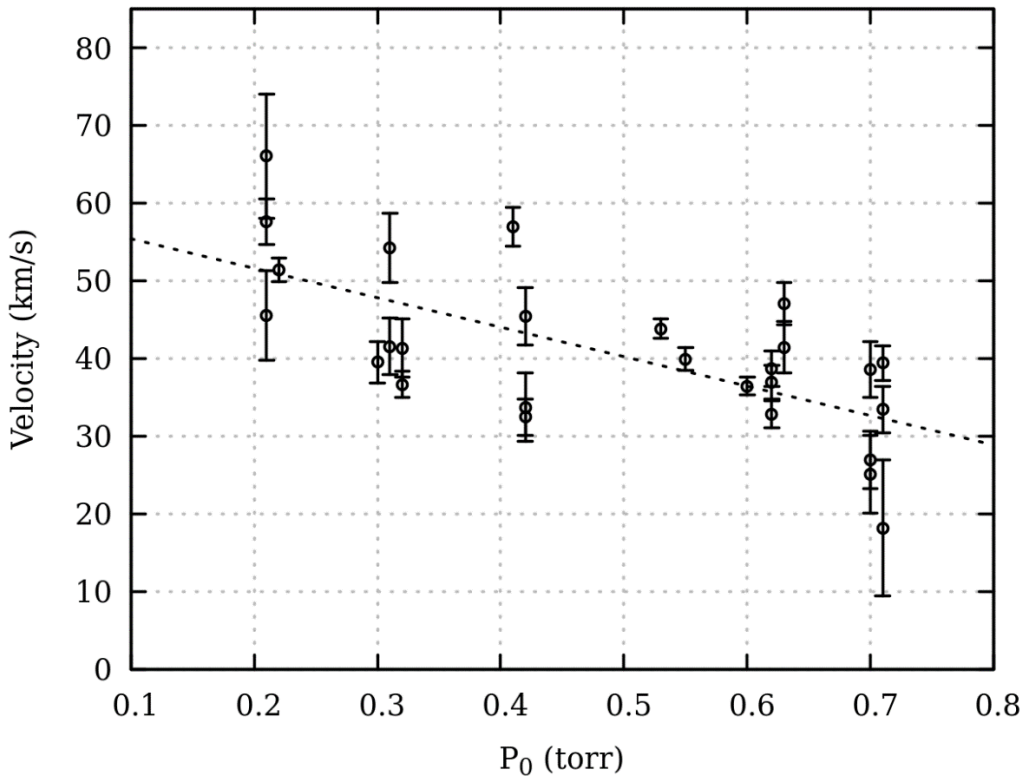

Figure 12. Axial sheath velocities measured at the end of the rundown phase shown as a function of Ne fill pressure. The dashed line is a linear fit to the data.

The measured axial velocity values are ~35% lower than the Lee model predicts (70 km/s) at 0.5 torr. This is possibly an indication that the mass sweeping and current factors (fm and fc, **Table 1**) can be further optimized, but also suggests the Lee model does not directly account for insulator geometry, which effectively imposes an offset for the starting sheath position (in the present study ~3 cm). This is likely the reason why the measured pinch time is similar to the Lee model despite the difference in axial velocity. Radial velocities for 0.5 torr are

calculated using the sheath positions/times in Figure 9 (i.e. across multiple shots), measuring 149±15 km/s, ~3.7x the average axial velocity at 0.5 torr of 40±4 km/s.

Capturing Sheath Liftoff

Figure 13 displays a multi shot collection of density maps showing liftoff of the current sheath from a smooth insulator for a fill pressure of 0.7 torr Ne. This pressure aided in the processing of the interferograms due to the increased density of the sheath, resulting in a greater signal to noise ratio.

Of note, as the sheath lifts off, its vertical displacement between 1.01 μs and 1.30 μs is ~1cm (estimated velocity: 30 km/s) so by 1.30 μs, the sheath has reached ~90 % of its peak axial velocity. Since the sheath does not lift off the insulator until ~0.8 μs, most of the sheath acceleration occurs close to the insulator shortly after lift-off. Typical current levels at liftoff are on the order of 25-35% of I_{max}. At 30% peak current the J x B force on the sheath should be near 10% peak force, so it is striking that the sheath reaches this velocity so quickly, but can be attributed to the low mass of the sheath in its formative state. Here the mass of the sheath at 1.01 μs is ~20% the mass at 1.30 μs evaluated from the analyzed interferograms. Over this same time period, the sheath is also propagating away from the insulator and towards the outer cathode at a reduced speed before the anode is directly bridged to the cathode rods.

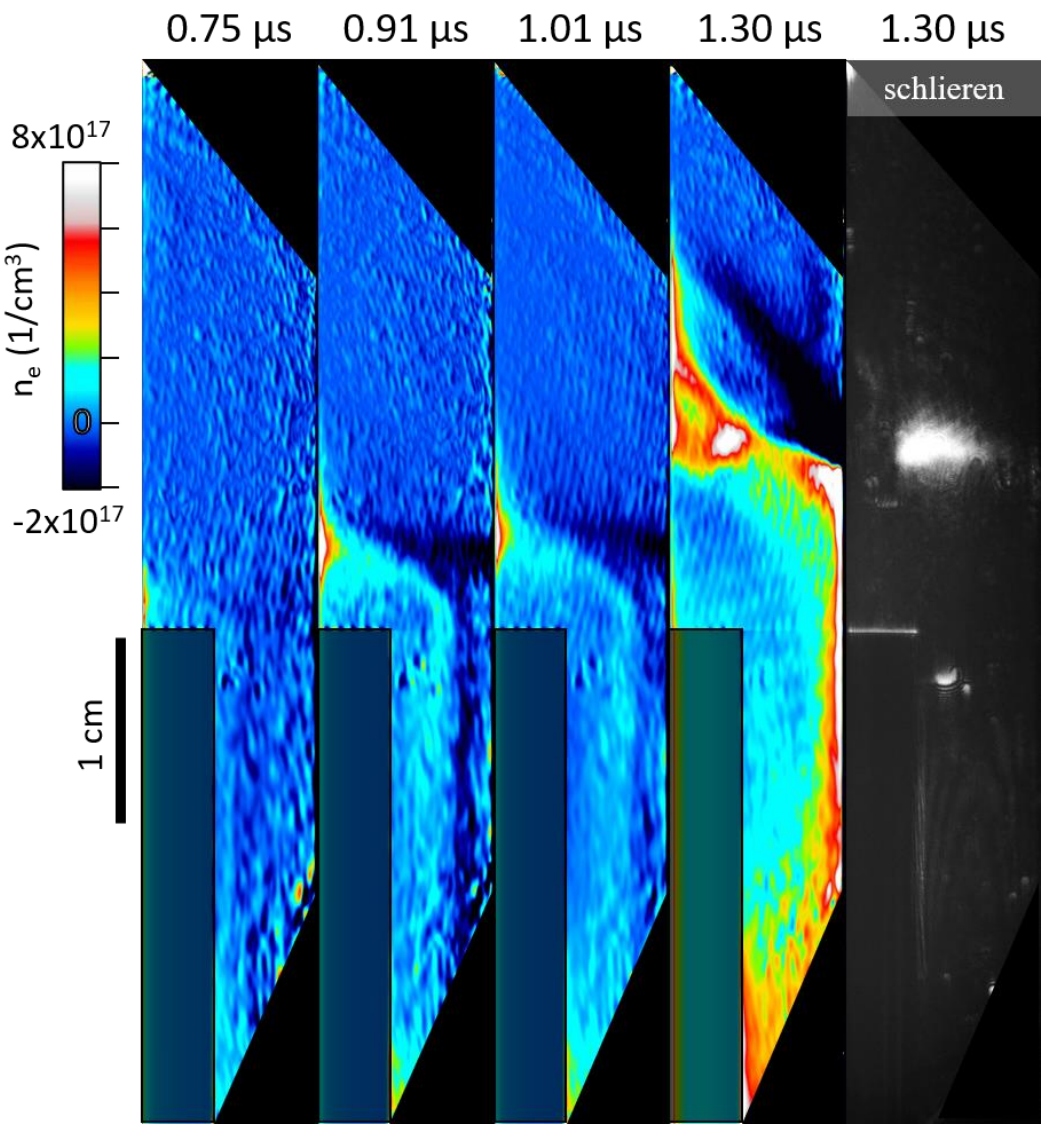

Figure 13. Time evolution (taken over multiple shots) of the plasma density from interferograms near the insulator surface, showing the liftoff of the plasma sheath from the insulator as it begins to propagate down the gap between the electrodes. All images are from shots taken at 0.7 torr fill pressure. The analysis results show some areas with negative density, the value of which gives an estimate of the error associated with these calculations. These areas are attributed to the inability to separate phase shift due to two separate effects: the electron density of the plasma and the density differences in the neon fill gas.

Plasma Temperature

The plasma temperature can be estimated from the current and line density of the pinch. This makes the Bennett relation,[36]

$$8\pi N_i k_B (ZT_e + T_i) = \mu_0 I^2,$$

remarkable. Here N_i, represents the ion line density; k_B, the Boltzmann constant; Z, the ionic charge number; T, temperatures of the plasma; μ_0, permeability of free space; and I, the current through the pinch. The electron line density,[37]

$$N_e = 2\pi \int_0^R r\, n_e(r)\, dr = 2\pi\,(1\times 10^{19}\mathrm{cm}^{-3})(1/2)(1\times 10^{-3}\mathrm{m})^2 = \pi\,(1\times 10^{19}\mathrm{m}^{-1}),$$

is related to the ion line density by a factor of the ionic charge number and can be estimated, in this case, by assuming n_e = 1 x 10^{19} cm^{-3} and a pinch radius, R, of 1 mm. Inverting the Bennett relation and assuming both $T_e = T_i$ and $Z = 10$ gives the framework for estimating the temperature with this expression:

$$T = \frac{Z\mu_0 I^2}{8\pi(Z+1)N_e k_B} = \frac{(4\pi\times 10^{-7}\mathrm{H/m})(2.5\times 10^5\mathrm{A})^2}{88\pi(\pi\times 10^{19}\mathrm{m}^{-1})\,(1.38\times 10^{-23}\mathrm{J/K})} = 6.6\times 10^6\mathrm{K} = 5.7\times 10^2\mathrm{eV}.$$

This provides an upper estimate of the temperature by assuming all the current in the anode flows through the pinch. The best fit between the Lee model and experimental current traces suggest 65% of the current conveyed by the anode flows through the pinch. With this current adjustment the plasma temperatures are tabulated for various ionization states and are found in the second column of **Table 3**. **Figure 14** suggests LTE and non LTE ionization states for these calculated temperatures, shown in the third and fourth columns of **Table 3**.

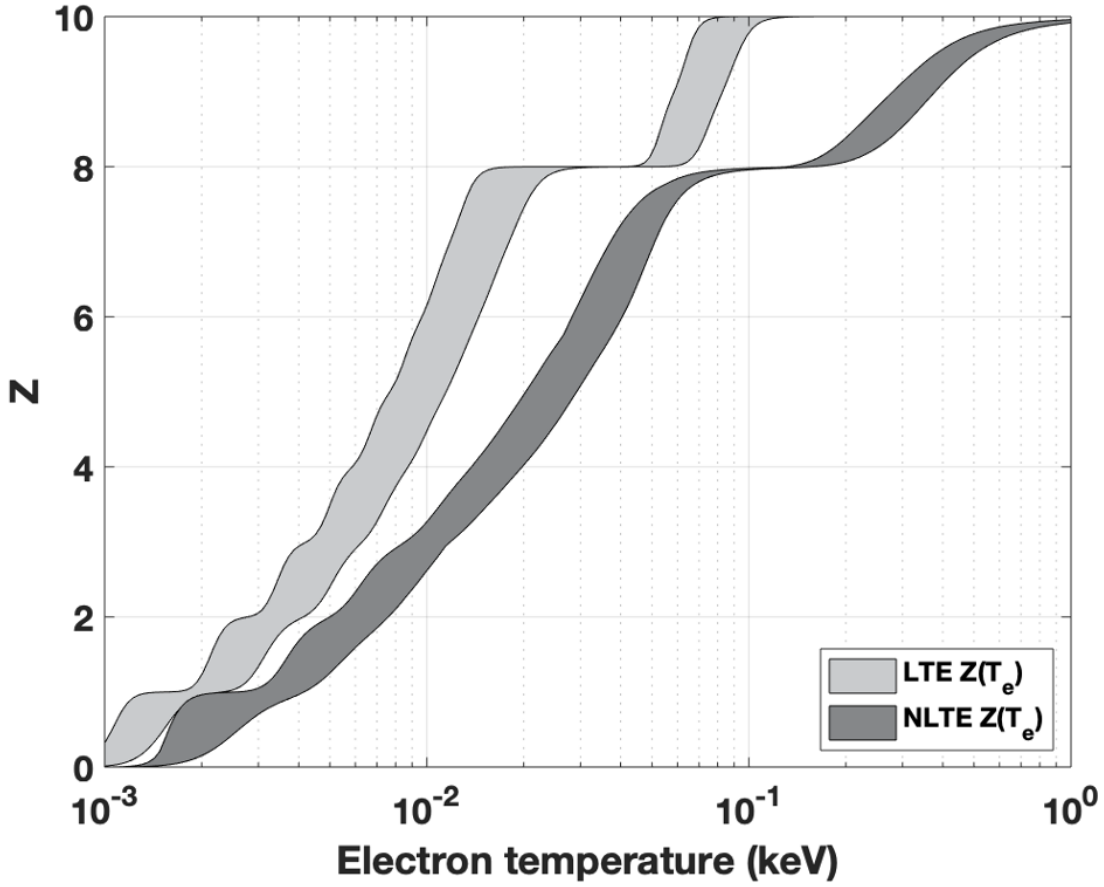

Figure 14. Ionization states of neon as a function of temperature obtained from PrOpacEOS for both LTE and NLTE based calculations.

Table 3. Neon plasma temperatures calculated for each ionization state and the predicted LTE and NLTE ionization state associated with each temperature as inferred by the Figure 14.

$Z_{assumed}$	T_{pinch} (eV)	Z_{LTE}	Z_{NLTE}
1	131	10	8
2	175	10	8
3	197	10	8
4	210	10	8
5	219	10	8
6	225	10	8
7	230	10	8
8	233	10	8
9	236	10	8
10	239	10	8

While the upper bound on the neon plasma temperature in the pinch is ~570 eV the best agreement between the ionization charge numbers and the LTE and NLTE predicted ionization charge numbers suggests a neon plasma pinch temperature in the 233 – 239 eV range.

Chapter 4 Surface Conditioning Study

According to theory and simulation of insulator flashover (Yordanov[14,14] and Seng[16,17]), breakdown is thought to begin with a group of high energy electrons emitted from the cathode plate at the exterior surface of the insulator. These electrons are accelerated by the high electric fields at the leading edge of the initial cathode electron emission and catalyze the ionization of fill gas that is then left in their wake. Several investigations of isolated insulator flashover have been reported in literature with several reports taking into consideration effects such as surface structure[38,39,40,41]. Based on these models, simulations, and experiments, it is expected that the flow of initial high energy electrons will be disrupted by surface conditioning. Horizontal structures are expected to delay the progression of the electron cascade by serving as deep traps[41]. The directionality of the surface conditioning will also encourage the cascade of electrons in a particular direction[38]. For example, vertical insulator surface structures would be expected to channel the electron cascade encouraging it to form more quickly in the axial direction, yet inhibit an even azimuthal distribution.

Insulator surface cascade theory could explain why there is a balance between having an insulator "broken in" before it gives optimal performance, but also that it must be retired after a certain number of shots to maintain performance. This is especially applicable to surface conditioned insulators that have a reduction in surface charge accumulation[39]. Additionally, surface conditioning may affect how Cu deposits are distributed on the surface, and in turn affect the dynamics of the electron cascade. While initial Cu deposits may improve the formation of the sheath at the insulator surface, excess deposits may lead to current leakage behind the plasma sheath and reduce the power coupled to the pinch.

A key result from Yamamoto et al.[42] also shows that surface roughness increases the variability of the flashover voltage in addition to increasing the flashover voltage with increasing roughness[42]. This provides a likely explanation for why the sheath is more azimuthally non-uniform in its progression. Other studies have shown that non-uniform discharge during the breakdown phase persists through to the final compression, resulting in lower density and lower neutron yields[43]. Complementary research has shown that promotion of pre-ionization via radiation demonstrated that greater breakdown uniformity results in increased focusing amplitude and thus greater X-ray yields[44]. In summary, moderate surface modifications, such as those applied here, are sufficient to delay (~100 ns) and disrupt azimuthal breakdown symmetry with effects on pinch dynamics.

The fill gas will have a bearing too, since it can influence the number of electrons available for the cascade. This theory corroborates the tenuous nature under which hydrogen current sheaths are observed in this system as compared to the Ne current sheaths which appear to have higher electron densities and produce schlieren images with higher contrast. The shifts in phase are also more exaggerated in the case of Ne current sheaths when compared to deuterium. Both these effects suggest higher electron densities in Ne current sheaths.

The geometry of the surface structuring may matter. Because these high energy electrons have a directionality there may be orientations of the surface conditioning structures that certain geometries may produce larger "electron cascade shadows." This effect would be true in a vacuum, but the extent to which the fill gas changes the picture is unclear.

Preparation of Borosilicate Insulator Surfaces

To investigate surface structure effects, smooth borosilicate insulator sleeve surfaces (Figure 15(a)) were modified by machining grooves into the surface or by adding surface roughness with sandpaper. Specifically, four modified surface structures were created for study (shown in Figure 15): (b) four horizontal grooves cut into the exterior of the insulator sheath at ¼" increments from the top, Exterior (H); c) four horizontal grooves cut into the interior of the insulator sheath at ¼" increments from the top, Interior (H); d) insulator sanded with 400 grit sandpaper using horizontal action, Exterior (H-S); and e) six vertical grooves cut into the exterior of the insulator sheath at 60^{o} azimuthal increments, Exterior (V). Modifications are denoted by their location either on the interior or exterior of the insulator relative to the anode in addition to (H) and (V) corresponding to horizontal or vertical respectively, while (S) represents the sanded condition. The directionality of the surface conditioning is expected to enhance (vertical) or hinder (horizontal) the cascade of electrons during breakdown. Fewer than 100 shots were taken on each insulator to minimize any effect of Cu deposition upon the insulator surface.

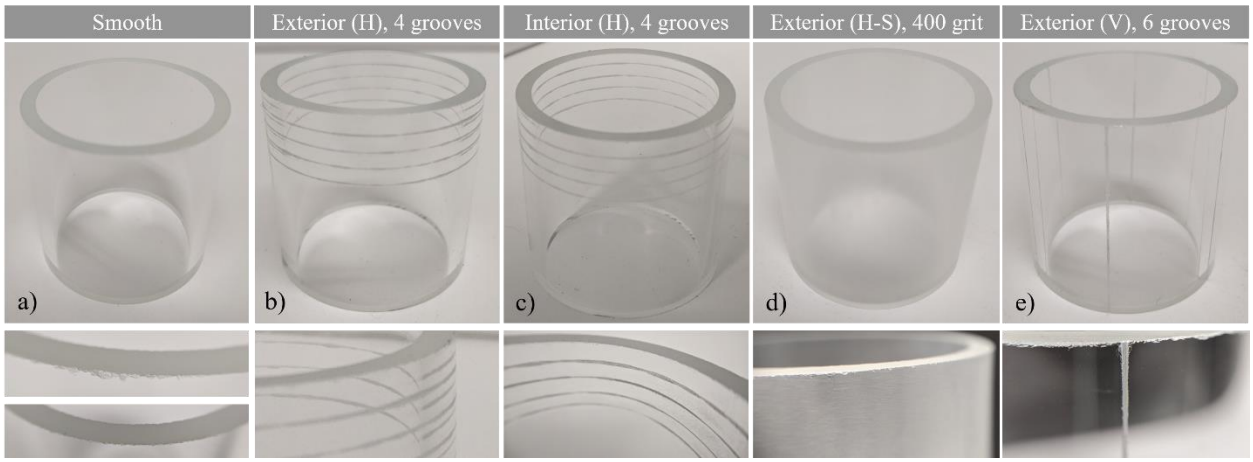

Figure 15. Borosilicate insulators and their surface features (from left to right: smooth finish—as received from the manufacturer, exterior horizontal grooved, interior horizontal grooved, exterior horizontal sanded with 400 grit, and vertical exterior grooved) For scale these insulators have a nominal 1 ¾ inch OD and $^{1}/_{8}$ inch wall thickness.

Pinch Structure Variations with Insulator Surface Conditioning

Figure 16 shows schlieren images for each insulator sleeve corresponding to the time closest to the pinch (rows a-b) and ~60 ns after pinch (row c) for a fill pressure of 0.5 torr. Above the image the average signal across all shots for the insulator from the Al-filtered photodiode is shown. It is clear from these images that the axis of collapse is non-uniform for insulators with structures on the exterior surface. The intensity of the X-ray signals for the smooth insulator is 7.23 ± 6.23 V; Exterior (H) = 1.12 ± 0.29 ; Exterior (H-S) = 3.58 ± 7.65; Exterior (V) = 3.10 ± 5.51; and Interior (H) = 3.58 ± 7.65. For straightforward comparison, the relative intensity of the X-ray signals normalized to the smooth insulator are: Exterior (H) = 0.15 ± 0.04; Exterior (H-S) = 0.17 ± 0.03; Exterior (V) = 0.43 ± 0.76; and Interior (H) = 0.50 ± 1.05. Here the ± represents the standard deviation of the signal and indicates that values with greater standard deviation than the average are indicative of significant outliers in yield or highly variable performance. This demonstrates surface characteristics of the insulator have significant influence on pinch X-ray yield, specifically machining structures in insulator surfaces reduces X-ray yield in the pinch. This could be due to the high energy electrons that roll off the surface of the insulator continue down the length of the anode magnetically insulated from it, U-turn at the tip and bore into the anode on axis. The result would be the continued ionization of the fill gas in the wake of these electrons preceding the current sheath as well as a plasma plume rising from the tip of the anode. Each of these effects could influence the pinch, however, the direct effect on X-ray or neutron yield is not clear. The surface conditioning of the insulator would affect the yield by affecting the roll off of the electrons from the surface of the insulator.

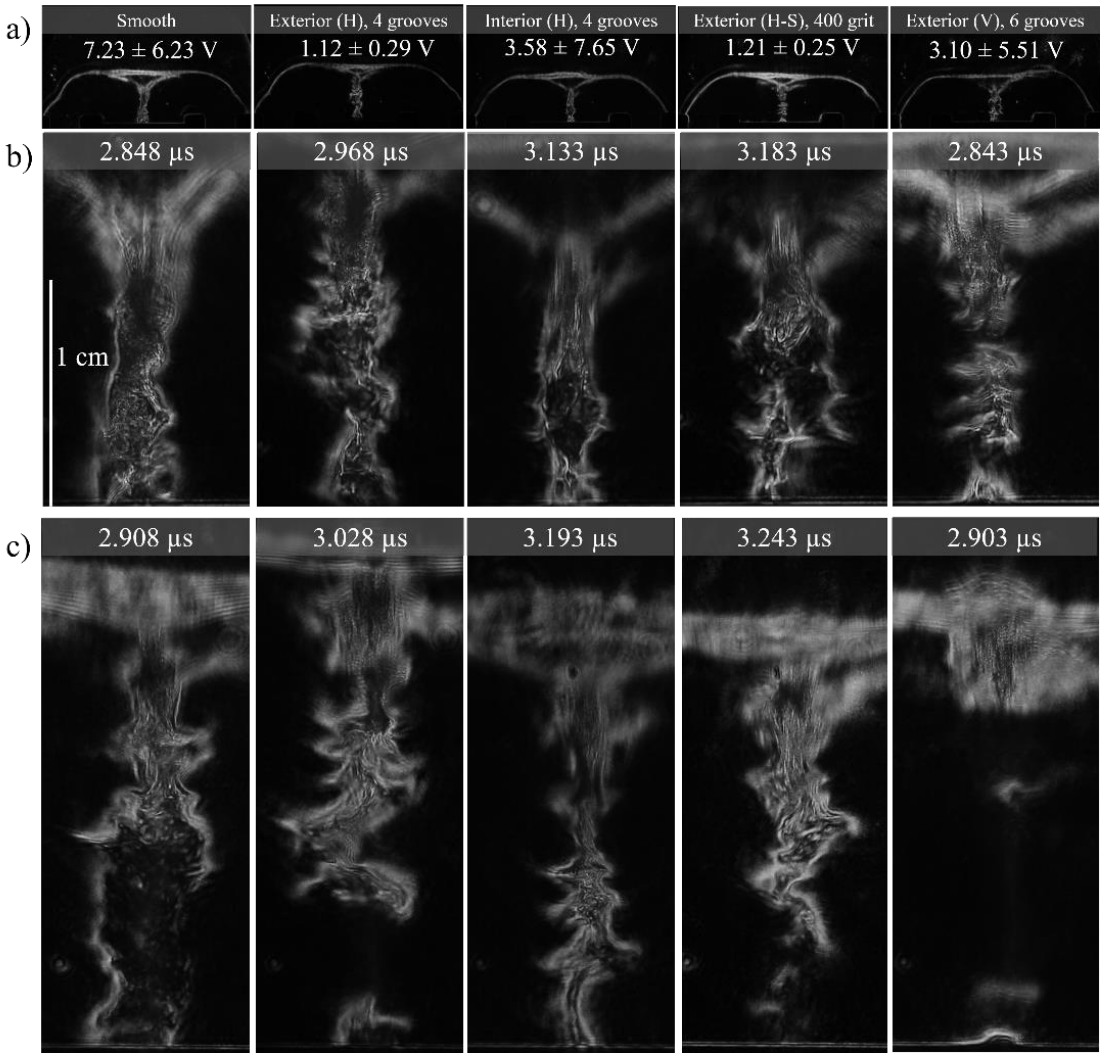

Figure 16. Characteristic schlieren images of the pinch. Each column displays multiple images from one shot: full sheath in the pinch region (top row), close up of plasma column early by 60 ns (middle row), and detail of column shown in top row (bottom row). Values report associated x-ray yield (top row) and backlight timing (lower rows) relative to the current start time. These shots vary with borosilicate insulator surface conditioning (as noted at the top of each column).

This delay, though small, is what the electron cascade over the surface of the insulator during breakdown would predict. The flow of high energy electrons gliding over the surface of the insulator would be disrupted by horizontal grooves and could leave areas void of ionized atoms and increase the effective surface area over which breakdown must fully develop. This would increase the characteristic timescale for breakdown to complete and reduce the symmetry of the breakdown. Furthermore, horizontal grooves should also help mitigate current loss across

the electrode gap during later stages of DPF operation. The pinches resulting from insulators with surface conditioning tend to be less stable with more erratic and delayed breakdown as compared to smooth insulator shots. Both m = 0 (sausage type) and m = 1 (kink type) instabilities are manifest in these pinches. Specific regions of the pinch, such as the top portion, or areas of high instability, exhibit blurry and ill-defined boundaries. It is not yet clear if this is due to the plasma element being removed from the focal plane, motion blur, more diffuse density gradients, or some other effect.

Sheath Liftoff—Horizontal Exterior Grooved Insulator

Typically, lift-off of the current sheath is uneven with the presence of horizontal exterior grooves and results in off-axis, lower density pinches. If performance is measured by a metric affected by off-axis nature or electron density, then surface conditioning will influence performance. In the case of soft X-ray yield, even though symmetry is not a factor per se, the electron density and plasma temperature matter, and surface conditioning will reduce the soft X-ray yield. This conclusion is substantiated by the observation that the filtered X-ray pin diodes returned a 7.23±6.23 V signal when using a smooth insulator and a 1.12±0.29 V signal with the insulator conditioned with horizontal exterior grooves. If performance is measured by neutron yield (with deuterium as a fill gas), then a lower ion density, lower plasma temperature, or poorly aligned beams and targets are expected to reduce performance.

Figure 18 shows a time evolution of the breakdown and liftoff phase of the exterior horizontal grooved insulator, for direct comparison to Figure 13, the smooth insulator. In the horizontal grooved insulator case, the sheaths appear to be more uniform and thinner, whereas in the smooth insulator case, the sheath appears to be thicker but less uniform in density. However, as observed in Figure 19, the axial position of the sheath has more pronounced asymmetry in the

early stages of run-down for shots taken with the horizontal grooved insulator. This could result in pinch asymmetry considering the alignment of the pinched columns that are observed in these experiments. To emphasize this asymmetry, Figure 17 shows the time-integrated self-emission (filtered by 532 nm central wavelength, 3 nm FWHM line filter) of a high yield and a low yield shot for each of the two primary insulators under investigation.

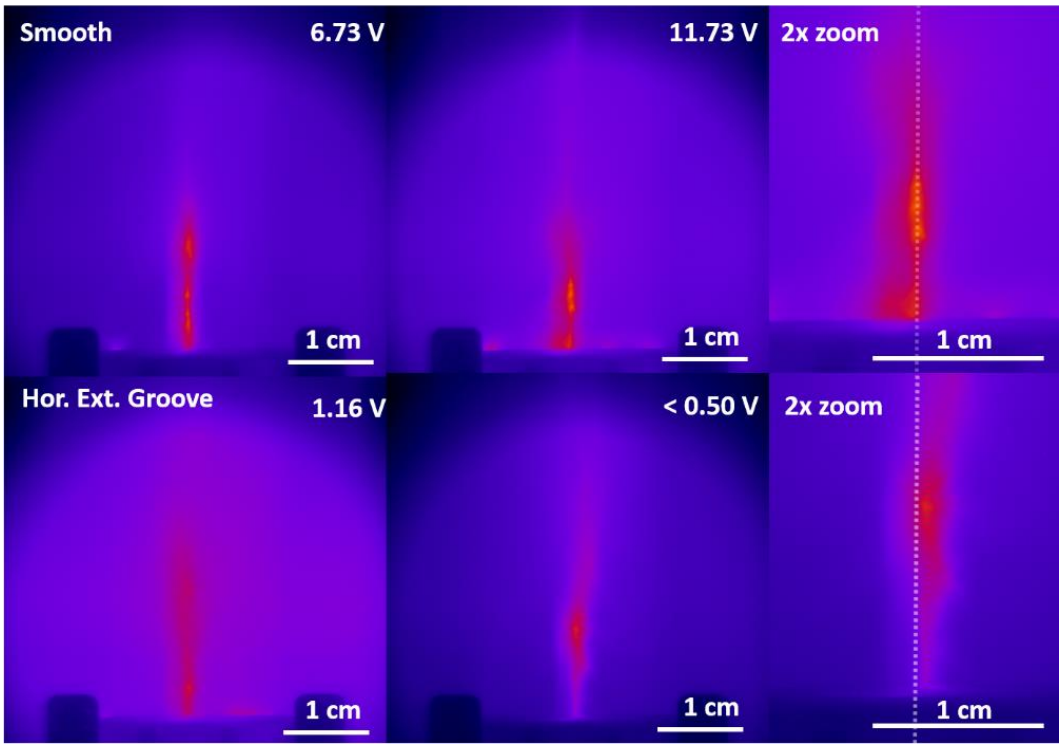

Figure 17. False-color, time-integrated, self-emission of Ne filtered by a 532 ±3 nm line filter. Self-emission in this range from warm Ne (~2 eV) results from several transitions corresponding to the family of 2s22p5–2s2sp54d and 2s22p5–2s2sp55d states. Two representative shots each from the smooth and horizontal exterior grooved insulator are shown, with a magnification of the brightest and dimmest shots given on the far-right column. The voltage listed for each image is the voltage from the photodiode; high voltages are indicative of high yield shots.

Figure 17 illustrates that the plasma columns with the horizontal grooved insulator tend to be off-axis and less bright. As shown previously in Figure 16, the pinches also appear to have a more kinked structure, which has previously been correlated to lower soft X-ray yield[45]. This is most likely indicative that the radial convergence is asymmetric, resulting in off-axis collapse of the column rather than the development of m=1 instabilities, but the two cannot be differentiated

based on present observations. The self-emission from the smooth insulator sleeve also shows distinguished hot-spots on axis, a feature absent from the horizontal grooved insulator.

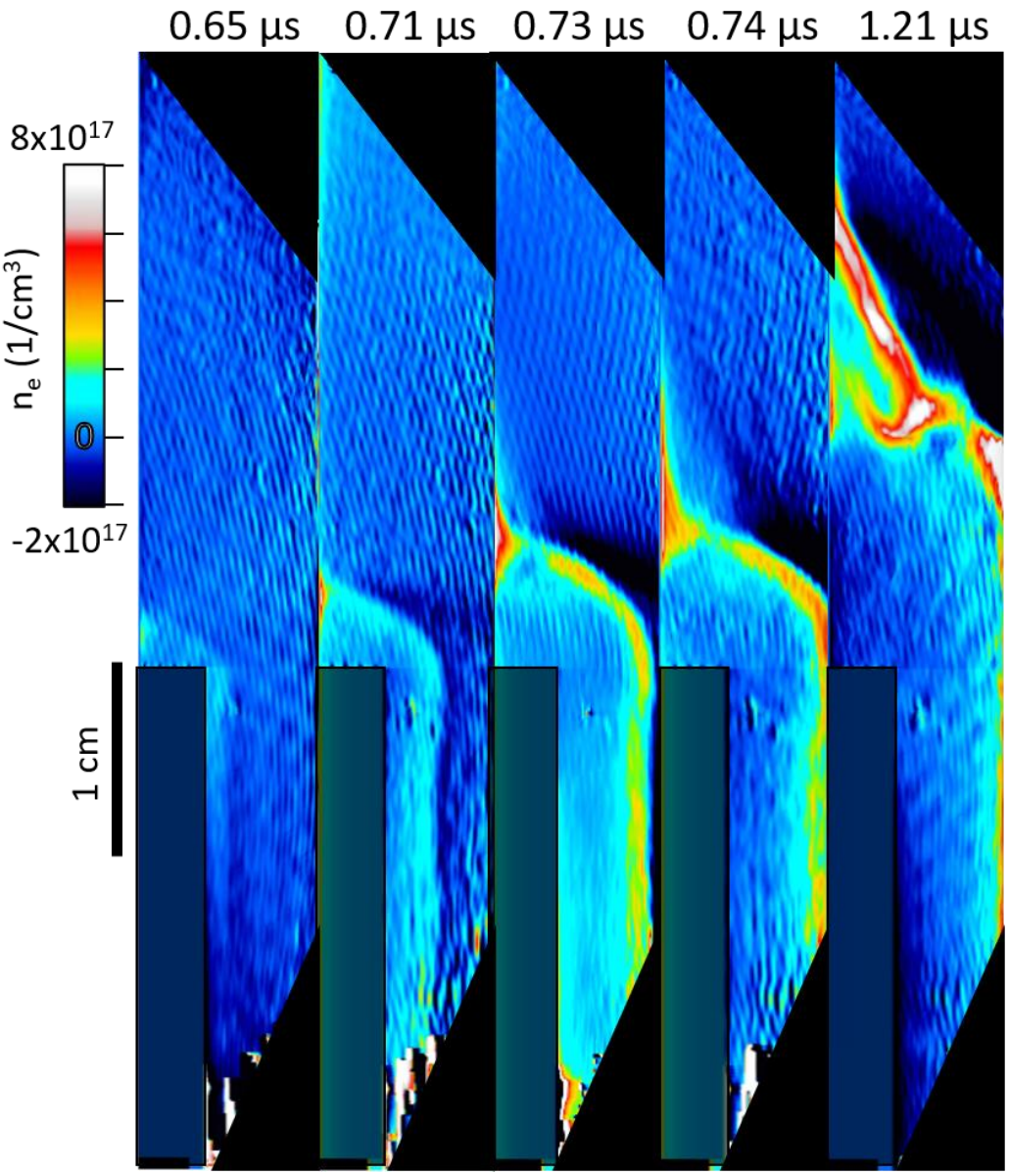

Figure 18. Time sequence (taken over multiple shots) of the plasma density from interferograms near the insulator surface for the exterior horizontal grooved insulator, showing the liftoff of the plasma sheath from the insulator as it begins to propagate down the gap between the electrodes. All images are with 0.7 torr Ne.

From the perspective of the breakdown across the insulator, it was hypothesized that horizontal grooves would increase the effective path length over which surface breakdown occurs, resulting in more difficult breakdown. Likewise, horizontal grooves should also help

mitigate current loss across the electrode gap during later stages of DPF operation. Measured sheath velocities at 0.5 torr for exterior structures are 50±9 km/s, and 48±10 km/s for interior structures. These values are similar to the axial sheath velocities for the smooth insulator, 45±12 km/s. Sheath lift-off time occurs ~100 ns earlier for the exterior horizontal grooved insulators.

Effect of Breakdown on the Pinch

Several differences in the sheath and pinch structure can be observed in electron density map comparisons of the smooth and the horizontal exterior grooved insulator shots shown in Figure 19. These interferograms are representative of the shots taken for these insulator cases.

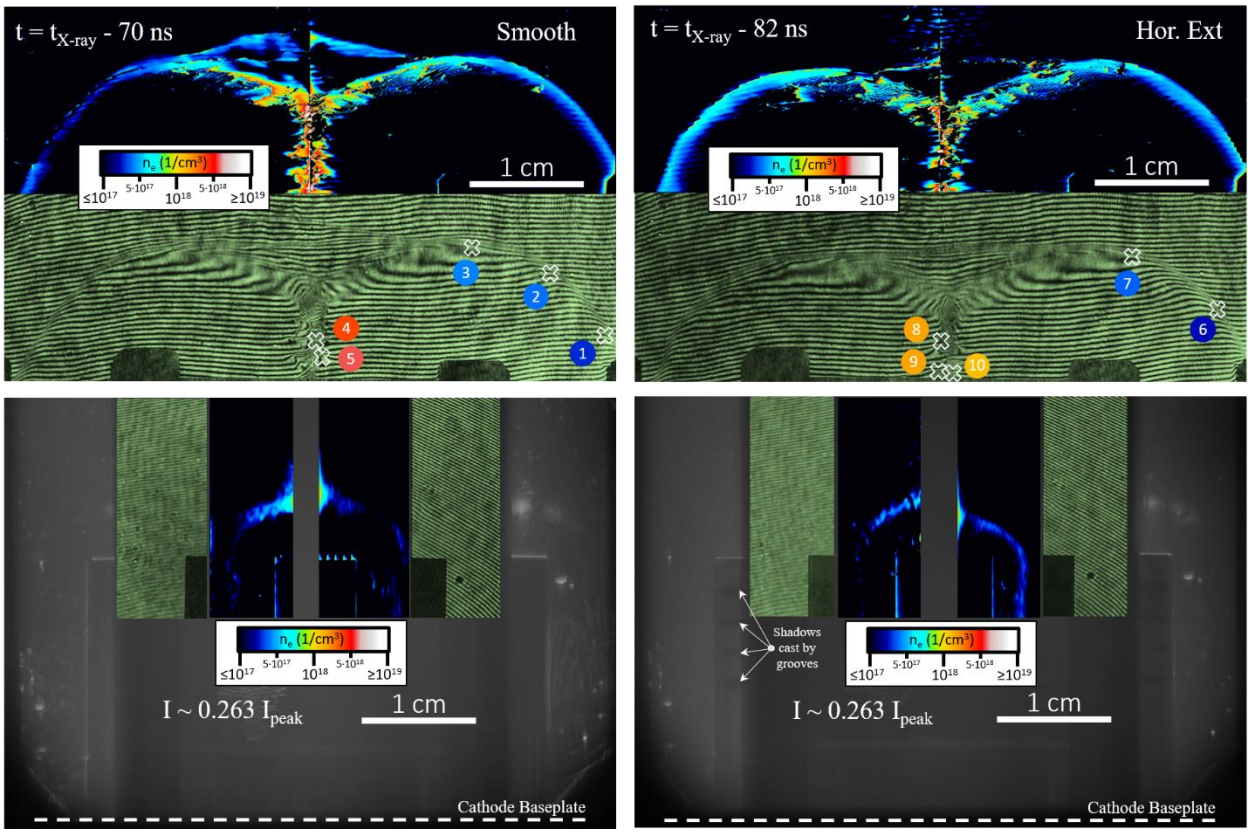

Figure 19. Comparison of Smooth and Horizontal Exterior Grooved Insulator sleeve, same-shot optical diagnostics for operation at 0.7 torr. The left-hand side figure showing the smooth insulator has been reproduced from Figure 8 for direct comparison. Analyzed results are false-colored on a log scale according to their electron density with units of cm^{-3}. Points selected for density analysis are marked by white X's and a corresponding tag is colored according to density with values given in Table 2 for the smooth and exterior horizontal grooved insulator respectively.

First, the sheath position shown in the breakdown region for the horizontal grooved insulator case is not symmetric about the axis, suggesting that local non-uniformities in the surface can impact sheath liftoff and produce pinches slightly off-axis. Second, at comparable timing, the resultant density immediately surrounding the tightest part of the pinch is less dense, although within an order of magnitude of the smooth insulator. It is acknowledged that both frames contain broken fringes that may lead to underestimation of the density in the surrounding fringes.

Chapter 5 Conclusions and Future Work

The motivation for this work began from the absence of satisfying answers in literature on the physics behind the plasma evolution in the DPF. Two areas that needed more investigation were, first, the correlation between the initiation of the plasma sheath and pinch dynamics and second, the role of the pinch in acceleration of ions and electrons. The work presented here seeks to address the dependence of pinch conditions on the initiation of the current sheath but even now the investigation is far from complete.

Accomplishments

A 4.4 kJ DPF system has been designed, built, and optimized for X-ray yield at 0.6 torr Ne fill gas and produces 0.24 J on average and in excess of 1 J for the best shots. The pinch has a lifetime ~60 ns and peak electron densities measured are >1 x 10^{18} cm^{-3} when using a smooth borosilicate insulator. The semi analytic Lee model was employed to guide design and optimization decisions.

The objective of this project was to collect comprehensive data sets on a wide array of diagnostics for each shot. This enables correlation between initial conditions and later characteristics of the plasma and performance yields without the complication of shot-to-shot variation. A voltage divider was built to capture voltage meausurements. Rogowski coils were built and calibrated to measure the current. A wide range visible spectrometer was fielded to inform fill gas makeup and infer plasma temperature. PIN photo diodes were fielded with filters ready to configure as Ross filter pairs when utilizing Kr, Ar, or Xe fill gas or dopants. Dual optical laser probing systems were designed, built and fielded enabling schlieren and/or interferometry imaging. The laser backlight strobes with 10 ns FWHM at 532 nm to provide 25

μm resolution in the 2D images and with a polarized delay leg can collect two frames separated in time (0-100ns) to capture the evolution of the pinch region. The interferometry fringes provide density description and schlieren images communicate gradient information to inform and benchmark simulation.

Others in the research group have performed Hydra simulations of this DPF so simulations can be readily run for upcoming configurations. Simulations to date have been benchmarked against baseline performance and characterize the possible effects of deuterium fill gas with dopants.

Conclusions

The dynamics of the DPF plasma sheath were studied using multi-frame laser probing at the insulator region and the pinch region on a same-shot basis, to correlate properties of the initial stages of the discharge with the pinch characteristics. The data from these experiments demonstrate that surface characteristics of the insulator have significant influence on the pinch and X-ray production. Reduced densities, increased pinch asymmetries, and reduced X-ray yields are observed when like insulators with modifications to the surface structure are used. The reduction in performance can be attributed to the performance of the initial breakdown phase, where surface structures suppress and vary the flashover at the insulator surface. This is likely due to the disruption of the flow of the high energy electrons that traverse the surface of the insulator at the onset of breakdown and lower excess surface charge, although these are inferred from theory and prior research of flashover behavior. Surface structures thus encourage uneven sheath formation leading to imbalances in the sheath structure that persists through the pinch with measurable changes in the resulting X-ray yield. Although the results reported here are

negative in nature (i.e. degrading rather than enhancing X-ray yield), insulator sleeve materials used across DPF devices will have imperfections that result from fabrication and machining, suggesting that the notorious shot-to-shot DPF performance issues may (in part) stem from manifestations of defects on the insulator surface and the early stages of discharge.

Future Work

Arguably the most significant improvement to the DPF machine that could be done would be to reiterate the design of the switch to improve timing jitter and increase energy delivered. An improvement in switch reliability would decrease changes in the inductance of the overall system between shots and give more reproducible circuitry performance in the main power feed. The plasma within the switch itself when triggered over time shears the pins that hold the switch electrodes in place, thus introducing variability in switch performance.

Next steps in the research would include extension of the current study to include effects on neutron yield. A suite of neutron diagnostics that includes an nTOF PMT detector and a Be activation counter are being fielded and calibration of the latter is currently in progress. The addition of an XUV framing camera with the ability to capture multiple frames would provide a characterization of the self-emission of the plasma. The challenge of adding this diagnostic is that the current level of noise interferes with triggering the XUV camera properly, so a reduction of noise would be necessary. Microscopic analysis of insulator surface after initial conditioning and at regular intervals throughout insulator usage would provide information about the evolution of surface insulator deposits and allow correlation between evolution of deposits and DPF performance. There has been difficulty finding a microscope that can accommodate the sample without compromising it. It would also be interesting to see if DPF performance could

be controlled through micro structures and coatings on insulator surface. A relatively easy improvement would be to add two more probing paths of the pinch region so there could be six images collected for each shot, better illuminating the evolution of the plasma in the pinch region.

MHD could be further used to understand effects of possible future insulator and electrode configuration. PIC simulation capability would be helpful to add to the modeling of this machine. However, computationally PIC simulations are very expensive.

Additional work might include ion detection and spectrometry[46]; installation of B-dot arrays to measure current profile and leakage; Zeeman spectroscopy on breakdown, axial and pinch phases to give an estimate of the magnetic field strength; impose external magnetic fields to study effects on run down velocity and pinch stability; addition of gas puff capability to enable a platform to study hybrid liner/shell dynamics in the context of a DPF; design and develop Faraday rotation polarimetry to measure magnetic field distribution[47]; and field a Thompson scattering set up to measure electron velocity distribution directly[48].

This thesis, in part is currently being prepared for submission for publication of the material. Housley, David; Hahn, Eric N.; Conti, Fabio; Narkis, Jeff; Beg, Farhat, N. The thesis author was the primary investigator and author of this material.

References

[1] Potter, D., "The formation of high-density z-pinches," Nucl. Fusion 18, 813 (1978).

[2] Krishnan, M., IEEE Trans. Plasma Sci. 40, 3189 (2012).

[3] Bernard, A., P. Cloth, H. Conrads, A. Coudeville, G. Gourlan, A. Jolas, Ch. Maisonnier, and J.P. Rager, Nucl. Instrum. Methods 145, 191 (1977).

[4] Mather, J.W. and P.J. Bottoms, "Characteristics of the dense plasma focus discharge," Phys. Fluids 11, 611 (1968).

[5] Gerdin, G., W. Stygar, and F. Venneri, "Faraday cup analysis of ion beams produced by a dense plasma focus," J. Appl. Phys. 52, 3269 (1981).

[6] Bures, B.L., M. Krishnan, R.E. Madden, and F. Blobner, "Enhancing neutron emission from a 500-J plasma focus by altering the anode geometry and gas composition," IEEE Trans. Plasma Sci. 38, 667 (2010).

[7] Serban, A., "Anode Geometry and Focus Characteristics," PhD diss., 1995.

[8] Zakaullah, M., I. Ahmad, G. Murtaza, M. Yasin, and M.M. Beg, "Effect of insulator sleeve contamination on the low energy plasma focus performance," Fusion Eng. Des. 23, 359 (1994).

[9] Shyam, A. and R.K. Rout, "Effect of anode and insulator materials on Plasma Focus sheath (pinch) current," IEEE Trans. Plasma Sci. 25, 1166 (1997).

[10] Beg, F.N., M. Zakaullah, G. Murtaza, and M.M. Beg, "Effect of insulator sleeve material on neutron emission from a plasma focus," Phys. Scr. 46, 152 (1992).

[11] Rout, R.K, A.B. Garg, A. Shyam, and M. Srinivasan, "Influence of electrode and insulator materials on the neutron emission in a low energy plasma focus device," IEEE Trans. Plasma Sci. 23, 996 (1995).

[12] Hussain, S., M. Shafiq, M.A. Badar, and M. Zakaullah, "Effect of insulator sleeve material on the x-ray emission from a plasma focus device," Phys. Plasmas 17, 092705 (2010).

[13] Feugeas, J.N., "The influence of the insulator surface in the plasma focus behavior," J. Appl. Phys. 66, 3467 (1989).

[14] Yordanov, V., D. Genov, I. Ivanova-Stanik, and A. Blagoev, "Ionization growth in the breakdown of plasma focus discharge," Vacuum 76, 365 (2004).

[15] Yordanov, V., I. Ivanova-Stanik, and A. Blagoev, "PIC-MCC method with finite element solver for Poisson equation used in simulation of the breakdown phase in dense plasma focus devices," J. of Physics: Conf. Series 44, 215-220 (2006).

[16] Seng, Y.S., P. Lee, and R.S. Rawat, "Electromagnetic particle in cell modeling of the plasma focus: Current sheath formation and lift off," Phys. Plasmas 21, 023509 (2014).

[17] Seng, Y.S., "Electromagnetic Particle in Cell Modelling of Plasma Dynamics in Breakdown and Lift-off Phases of Plasma Focus," PhD diss., 2016.

[18] Feugeas, J. and O. von Pamel, "Current distribution during the breakdown in a coaxial electrode system," J. Appl. Phys. 66, 1080 (1989).

[19] Donges, A., G. Herziger, H. Krompholz, F. Rühl, and K. Schönbach, "The breakdown phase in a coaxial plasma gun," Phys. Lett. A 76, 391 (1980).

[20] Krompholz, H., W. Neff, F. Rühl, K. Schönbach, and G. Herziger, Formation of the plasma layer in a plasma focus device," Phys. Lett. A 77, 246 (1980).

[21] Scholz, M. and I.M. Ivanova-Stanik, "Initial phase in plasma focus device—model and computer simulation," Vacuum 58, 287 (2000).

[22] Zakaullah, M., A. Waheed, S. Ahmad, S. Zeb, and S. Hussain, "Study of neutron emission in a low-energy plasma focus with β-source-assisted breakdown," Plasma Sources Sci. Technol. 12, 443 (2003).

[23] Joe Kilkenny, HEDP Diagnostics Course, Spring 2020, lecture notes in possession of the author.

[24] Da Silva, L.B., T. W. Barbee, Jr., R. Cauble, P. Celliers, D. Ciarlo, S. Libby, R. A. London, D. Matthews, S. Mrowka, J. C. Moreno, D. Ress, J. E. Trebes, A. S. Wan, and F. Weber, "Electron density measurements of high density plasmas using soft X-ray laser interferometry," Phys. Rev. Lett. 74, 3991 (1995).

[25] Lee, S., "Plasma Focus Radiative Model: Review of the Lee Model Code," J Fusion Energ 33, 319–335 (2014).

[26] Wagner, T.C., W.A. Stygar, H.C. Ives, and T.L. Gilliland, "Differential-Output B-dot and D-dot monitors for current and voltage measurements on a 20-MA, 3-MV pulsed-power accelerator," Physical Review Special Topics-Accelerators and Beams, v. 11, 100401 (2008).

[27] Kramida, A., Yu Ralchenko, and J. Reader. "Team 2013, NIST Atomic Spectra Database," (Gaithersburg, MD: National Institute of Standards and Technology), Available: https://physics. nist. gov/asd (2019).

[28] Johnson, W.R., I. M. Savukov, U. I. Safronova, and A. Dalgarno, "E1 transitions between states with n= 1-6 in helium-like carbon, nitrogen, oxygen, neon, silicon, and argon," The Astrophysical Journal Supplement Series 141.2, 543 (2002).

[29] Henke B.L., E.M. Gullikson, and J.C. Davis, At. Data Nucl. Data Tables 54, 181 (1993).

[30] Beg, F.N., I. Ross, A. Lorenz, J.F. Worley, A.E. Dangor, and M.G. Haines, "Study of x-ray emission from a table top plasma focus and its application as an x-ray backlighter," J. Appl. Phys. 88, 3225 (2000).

[31] Wong, D., A. Patran, T.L. Tan, R.S. Rawat, and P. Lee, "Soft X-ray optimization studies on a dense plasma focus device operated in neon and argon in repetitive mode," IEEE Trans. Plasma Sci. 32, 2227 (2004).

[32] Kalaiselvi, S.M.P., T.L. Tan, A. Talebitaher, P. Lee, and R.S. Rawat, "Optimization of neon soft X-rays emission from 200 J fast miniature dense plasma focus device: A potential source for soft X-ray lithography," Phys. Lett. A 377, 1290 (2013).

[33] Bennett, N., M. Blasco, K. Breeding, V. DiPuccio, B. Gall, M. Garcia, S. Gardner, J. Gatling, E.C. Hagen, A. Luttman, and B.T. Meehan, "Kinetic simulations of gas breakdown in the dense plasma focus," Physics of Plasmas, 24(6), 062705 (2017).

[34] Schmidt, A., Link, D. Welch, B.T. Meehan, V. Tang, C. Halvorson, M. May, and E.C. Hagen, "Fully kinetic simulations of megajoule-scale dense plasma focus," Phys. Plasmas 21, 102703 (2014).

[35] Hirano, K., T. Yamamoto, K. Shimoda, and H. Nakajima, "Production of a highly ionized ion beam by a plasma focus," J. Phys. Soc. Jpn. 58, 3591 (1989).

[36] Bennett, W.H., "Magnetically self-focussing streams," Physical Review, 45 890 (1934).

[37] Haines, M.G., "A review of the dense Z-pinch," Plasma Phys. Control. Fusion, 53 093001 (2011)

[38] Victoria, R., L.E. Gockenbach, H. Borsi, H. Negle, and A. Lunding, "Effects of roughness on surface flashover voltages under DC stress," IEEE Annual Report-Conference on Electrical Insulation and Dielectric Phenomena, 576-579 (October 2007).

[39] Xue, J., H. Wang, J. Chen, K. Li, Y. Liu, B. Song, J. Deng, and G. Zhang, "Effects of surface roughness on surface charge accumulation characteristics and surface flashover performance of alumina-filled epoxy resin spacers, " Journal of Applied Physics, 124(8), 083302 (2018).

[40] Morita, H., T. Yokosuka, and A. Hatanaka, "Characteristics of electrical charging on smooth and rough surfaces of glass plates under vacuum," IEEE Transactions on Dielectrics and Electrical Insulation, 23(2), 1226-1232 (2016).

[41] Qiu, Y. and I.D. Chalmers, "Effect of electrode surface roughness on breakdown in SF6-N2 and SF6-CO2 gas mixtures," Journal of Physics D: Applied Physics, 26(11), 1928j (1993).

[42] Yamamoto, O., T. Satoh, H. Hayashi, S. Hamada, T. Kobayashi, H. Omura, and H. Morii, "Effects of roughening insulator surface on charging and flashover characteristics of a long glass insulator in vacuum," IEEJ Transactions on Fundamentals and Materials, 126(8), 769-774 (2006).

[43] Talebitaher, A., S.M.P. Kalaiselvi, S.V. Springham, P. Lee, T.L. Tan, and R.S. Rawat, "Laser Shadowgraphic study of the influence of krypton-seeding, switch synchronization and electrode geometry on plasma dynamic in plasma focus device," Journal of Fusion Energy, 34(4), 794-801 (2015).

[44] Khan, H.U., S.S.Hussain, M. Ikram, M.Z. Ilyas, M.Z. khan Niazai, and M. Shafiq, "Stable current sheath dynamics caused by preionization source in a small plasma focus device using He as an operating gas," Radiation Effects and Defects in Solids, 174(3-4), 273-283 (2019).

[45] Talukdar, N., N.K. Neog, and T.K. Borthkur, Effect of anode shape on pinch structure and X-ray emission of plasma focus device." Results in Physics, 3, 142-151 (2013).

[46] Zhou, O., D. Housley, F. Conti, and F.N. Beg. Detection of> 100 keV electron and ion emission from 10 kJ Dense Plasma Focus. APS (2019): JP10-070.

[47] I. H. Hutchinson, Principles of Plasma Diagnostics. Cambridge University Press, 2002.

[48] Milder, A. L., S. T. Ivancic, J. P. Palastro, and D. H. Froula. Impact of non-Maxwellian electron velocity distribution functions on inferred plasma parameters in collective Thomson scattering. Physics of Plasmas 26, no. 2 (2019): 022711.